A&A 371, 675–697 (2001)
DOI: 10.1051/0004-6361:20010387

Astronomy & Astrophysics

The Cygnus superbubble revisited

B. Uyanıker[1,2], E. Fürst[1], W. Reich[1], B. Aschenbach[3], and R. Wielebinski[1]

[1] Max–Planck–Institut für Radioastronomie, Postfach 2024, 53010 Bonn, Germany
[2] Dominion Radio Astrophysical Observatory, Herzberg Institute of Astrophysics, Penticton, B.C., Canada V2A 6K3
[3] Max–Planck–Institut für Extraterrestrische Physik, Postfach 1603, 85740 Garching, Germany

Received 18 January 2001 / Accepted 8 March 2001

Abstract. The Orion local spiral arm is seen tangential towards the Cygnus region. Intense radio emission with quite a complex morphology is observed, which appears to be surrounded by strong soft X–ray emission. This remarkable X–ray structure is known as the Cygnus superbubble. We compare a recent 1.4 GHz radio continuum and polarization map from the Effelsberg 100-m telescope with X–ray data from the ROSAT all–sky survey of this area. Including available survey data of the infrared, H I and CO emission, we investigate a number of high latitude features, which are physically related to one of the Cygnus OB associations. These OB associations, however, are located along the local arm at different distances. Our results support the view that the Cygnus superbubble is not a physical unity, but results from a projection of unrelated X–ray emitting features at different distances blown out from the local arm seen along the line of sight.

Key words. ISM: Cygnus superbubble – radio continuum: ISM – X–ray: ISM – galaxy: structure

1. Introduction

The radiation and wind from massive stars and supernova (SN) explosions determine the structure and energy content of the interstellar medium (ISM). Topologically, the ISM appears to be highly inhomogeneous. Much of its mass is concentrated in clouds with a small filling factor, whereas much of its volume is filled with warm inter-cloud gas (see Spitzer 1990 for a review). A hot gas component exists as well, which is generated by SN explosions and strong winds from massive stars (Cox & Smith 1974; McKee & Ostriker 1977; Ferrière 1995). This tenuous gas has a density of about 10^{-3} cm^{-3} and a temperature of about 10^6 K. Cool, dense clouds reaching a density of 10^3 cm^{-3} with a temperature around 100 K float in this hot material. These clouds are birth places for new stars. The new stars, when of type O or B, have strong winds. They burn their energy rapidly to become a supernova. In the vicinity of a massive star, either because of the strong wind or due to the explosion of the star, the surrounding ISM is blown off. In particular, the combined effects from SN explosions and stellar winds from OB associations produce quite large cavities filled with hot gas and are called "superbubbles". They are observationally traced at optical, radio and X–ray wavelengths. The origin of this hot gas has been the topic of numerous investigations including the interaction of the stellar winds with interstellar matter (Castor et al. 1975; Weaver et al. 1977; Abbott et al. 1981) and single or sequential SN explosions (Elmegreen & Lada 1977; Tomisaka et al. 1980; Higdon 1981).

When the extent of a superbubble becomes comparable to the thickness of the Galactic disc, it may break out of the disc and the hot gas will escape. A superbubble remains bound to the disc if its mechanical luminosity is around $L_{\rm SN} \leq 3\ 10^{37}$ erg s^{-1} in a uniform magnetic field as large as 5 μG (Tomisaka 1990; Tomisaka 1998; see also Ferrière et al. 1991, for the effect of magnetic fields on the evolution of superbubbles). Thus, the formation of a gaseous halo around a spiral galaxy is connected to the OB associations with a high star formation rate. The escaped hot gas might rise several kpc above the Galactic plane, where it cools radiatively. The cooled material falls back to the disc and can be observed as high velocity clouds (Bregman 1980). A study of superbubbles extending to high latitudes, therefore, provides useful information on the mutual relation between the disc and the halo of the Galaxy.

Three giant bubbles have been identified so far in the local arm of the Milky Way. These structures are known as Orion-Eridanus (Reynolds & Ogden 1979; Guo et al. 1995; Brown et al. 1995), Scorpio-Centaurus (Weaver 1979; Egger 1998) and the Cygnus superbubble (hereafter CSB, Cash et al. 1980) according to the constellations where they are located. Recently Heiles (1998) reported a possible bubble towards $\ell \sim 238°$ and $b \sim 9°$. While

---

Send offprint requests to: W. Reich,
e-mail: `wreich@mpifr-bonn.mpg.de`

Table 1. OB associations in Cygnus region. The table is a compilation from Humphreys (1978), Garmany & Stencel (1992), Bochkarev & Sitnik (1985), Sitnik & Mel'nik (1996) and Mel'nik & Efremov (1995)

name	ℓ (°)	b (°)	$\Delta\ell$ (°)	Δb (°)	dist[a] (kpc)	age[b] (Myr)
OB1	75.50	1.17	3.0	3.4	1.25–1.83	7.5
OB2	80.10	0.90	–	–	1.44–2.10	5.0
OB3	72.55	2.20	2.5	2.2	1.58–2.51	8.3
OB4	82.50	−4.30	3.0	2.0	1.0	[c]
OB5	67.10	2.10	5.8	9.6	[c]1.61	[c]
OB6	86.00	1.00	6.0	8.0	[c]1.70	[c]
OB7	90.00	2.05	12.0	13.9	0.74–0.80	13.0
OB8	77.75	3.75	2.9	3.3	2.19–2.32	3.0
OB9	78.00	1.50	2.0	1.4	1.17–1.20	8.0

[a] This column indicates the distance interval for a given OB association.

[b] Age obtained from the Hertzsprung-Russel diagram.

[c] Doubtful.

the Orion-Eridanus bubble has been identified by its Hα emission and the Sco-Cen bubble by its H I filaments, the CSB is identified by its strong X–ray emission. The CSB is the largest bubble. Its angular size is 18° × 13° along Galactic longitude and latitude, respectively. It is very complex and extends up to latitudes well above the local spiral arm. Numerous OB associations at different distances are located in its direction. The physical connection to the CSB is unclear. Therefore, the distance to the CSB is poorly known and its size and energetics remain uncertain (Ruprecht et al. 1981; Bochkarev & Sitnik 1985; Garmany & Stencel 1992; Comerón et al. 1998; de Zeeuw et al. 1999). Since the line of sight is along a spiral arm, the confusion of the various objects is large and the discrimination of individual structures is difficult.

In this paper we investigate the CSB and try to disentangle the superposition of structures along the local spiral arm by using new, sensitive radio continuum and polarization data at 1.4 GHz (Uyanıker et al. 1999; Reich et al. 1990), ROSAT all–sky survey data (Aschenbach 1993), IRAS 60 and 100 μm images (Beichmann et al. 1985), H I data from the Dwingeloo Survey (Hartmann & Burton 1997) and CO data at 115 GHz (Dame et al. 1987). The paper is organized as follows: in Sect. 2 we discuss the OB associations towards the CSB, their placement in the region and possible relations to the observed X–ray structures. In Sects. 3 and 4 effects of the stellar winds from the OB stars and the supernova initiated bubbles are briefly discussed. After these introductory sections we present the latest observational data of the Cygnus region from the Effelsberg 1.4 GHz survey and the ROSAT all–sky survey together with the IRAS, H I and CO data. Each data set is then discussed separately in Sect. 6–9 and an overview of the data together with a discussion on the nature of the CSB is given in Sect. 10. Our interpretation of the observed structures is given in Sect. 11.

Table 2. The list of H II regions, whose angular diameters are $\gtrsim 10'$, selected from the Sharpless catalogue (1959). The distances and $V_{\rm LSR}$ values are taken from the list of kinematically distinct H II regions of Brand & Blitz (1993). The distance estimate of S117, 0.5 kpc, is adopted from Straižys et al. (1989)

name	ℓ (°)	b (°)	diam (′)	dist (kpc)	$V_{\rm LSR}$ (km s^{-1})
S 92	064.08	+01.65	50		
S 94	064.93	+06.77	25		
S 96	066.10	+07.18	25		
S 97	066.87	+00.91	10	3.90	21.0
S 98	068.15	+01.02	15		
S101	071.58	+02.84	20	2.50	13.7
S102	071.41	−05.31	40		
S103	074.12	−08.33	210		
S105	075.46	+02.43	18		
S108	078.19	+01.81	180	1.5	
S109	079.49	+00.15	1080	1.4	
S110	079.60	−12.17	50		
S111	081.19	−17.01	90		
S112	083.78	+03.29	15	2.10	−4.0
S113	083.71	−08.25	15		
S115	084.84	+03.91	50	3.0	
S117	085.49	−00.99	240	0.5–0.8	0.0
S118	087.49	−08.92	480		
S119	087.60	−03.84	160	0.7	3.5
S123	091.15	−06.35	13		
S124	094.48	−01.54	70		
S126	095.39	−16.80	160	0.6	−0.2
S129	098.50	+07.97	140	0.4	−13.9
S131	099.29	+03.73	170		
S132	102.79	−00.65	90		

2. The relation of the Cyg OB associations to the Cygnus superbubble

The CSB was discovered by Cash et al. (1980) in the soft X–ray regime using the A-2 experiment on board the HEAO-1 satellite. They found a temperature of the emitting gas of $T = (1.6–2.5)\ 10^6$ K and a column density of $N_{\rm H} = (5.6–9)\ 10^{21}$ cm^{-2}, assuming a thermal spectrum from an optically thin hot plasma. They adopted a distance of 2 kpc for the X–ray structure, based on the high value of $N_{\rm H}$ obtained from the spectral analysis and a possible relation of the X–ray structure with the Cyg OB2 association (see Table 1). At 2 kpc the size of the CSB is 600 × 450 pc and the total energy content is 10^{54} erg, which is equivalent to the energy of about 1000 SN explosions.

Table 1 lists the known OB associations in the Cygnus region. OB5 is outside the CSB, and some of the others are at the CSB peripheries, e.g. OB6, OB7 (see Fig. 1 for a finder chart of the Cygnus region). The distances vary between 0.7 kpc to about 2.3 kpc. Has one of the associations within the CSB enough massive stars to excite the superbubble by winds or SN activity? Among the OB associations, Cyg OB2 seems to be the most probable candidate to power up the CSB: it contains at least

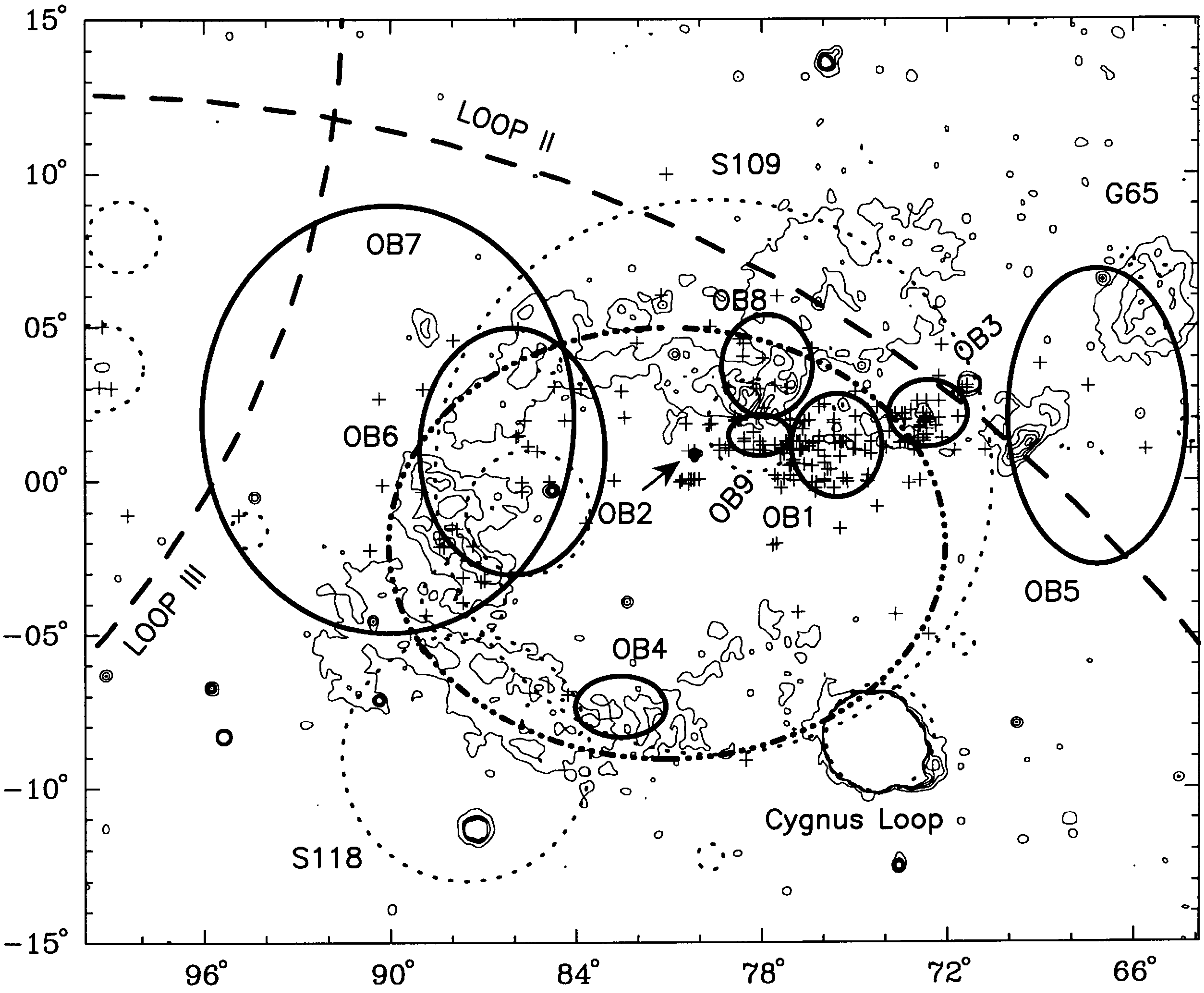

Fig. 1. Finder chart for the Cygnus region in Galactic coordinates. The thick dashed-dotted ellipse shows the location of the CSB and solid ellipses indicate the approximate position and extent of the OB associations. Thick dashed lines show the boundaries of the radio loops and plus signs mark the positions of the stars from the list of Garmany & Stencel (1992) and of candidate stars showing expansion (Comerón et al. 1998). The dotted circles denote the prominent H II regions given in Table 2. Thin line contours show the 3/4 keV ROSAT image, see text for details

3000 stars and about 300 of them are OB stars (Reddish et al. 1966; Humphreys 1978). Furthermore, about a dozen of the most massive stars known in the Galaxy are in this association (Abbott et al. 1981; Massey & Thompson 1991). Some of the stars in this association have been observed at radio wavelengths (Wendker & Altenhoff 1980; Abbott et al. 1981; Leitherer et al. 1984), in X–rays (Kitamoto & Mukai 1996; Waldron et al. 1998) and in γ–rays (Chen et al. 1996). Torres-Dodgen et al. (1991) estimated the distance and age of the Cyg OB2 to 1.7 kpc and 3 Myr, respectively.

Another problem in matching the observed X–ray structures with the OB associations is actually the difficulty in determining the distances, ages and the number of members of the associations. The age of OB associations derived from the main sequence turn off times of the stars (nuclear age from the stellar evolution obtained by counting the number of upper main sequence stars of the highest absolute magnitude) most likely overestimate the true age (see Tables 1 and 5 of Bochkarev & Sitnik 1985). The HIPPARCOS astrometric data, on the other hand, do not provide accurate enough kinematic ages (Brown et al. 1997); also the knowledge of membership and distance towards the Cygnus associations remained unimproved (de Zeeuw et al. 1999); for distances exceeding 500 pc the parallaxes are difficult to measure with the HIPPARCOS satellite. Comerón et al. (1998) discussed the discrepancies in determining the distances and Comerón et al. (1993) reported anomalous proper motions observed in the Cygnus region.

Table 3. List of supernova remnants in the Cygnus region. The columns, from left to right, contain information on the Galactic coordinates, angular size, the given name of the remnant and the available distance estimate. This list is largely based on the online catalogue of Green (2000). The distance estimates are adopted from various sources. The references are: a) Landecker et al. (1990), b) Lozinskaya (1981), c) Lozinskaya et al. (1993), d) Blair et al. (1999), e) Green & Gull (1989), f) Landecker et al. (1993), g) Landecker et al. (1980), h) Feldt & Green (1993), i) Tatematsu et al. (1980), j) Leahy & Aschenbach (1996), k) Landecker et al. (1999)

ℓ (°)	b (°)	size (′)	name	dist kpc	Ref
65.1	+0.6	90×50			a
65.3	+5.7	310×240	G65	0.8	b
65.7	+1.2	18	DA 495		
67.7	+1.8	9			
68.6	−1.2	28×25			
69.0	+2.7	80	CTB 80		
69.7	+1.0	16			
73.9	+0.9	22		1.3	c
74.0	−8.5	230×160	Cygnus Loop	0.44	d
74.9	+1.2	8×6	CTB87	12	e
76.9	+1.0	9×12		>7	f
78.2	+2.1	60	DR4, W66	1.5	g
82.2	+5.3	95×65	W63	1.3	d
84.2	−0.8	20×16		4.5	h
84.9	+0.5	6			
89.0	+4.7	120×90	HB21	0.8	i, j
93.3	+6.9	27×20	DA 530	3.5	k
93.7	−0.2	80	CTB 104A, DA 551		
94.0	+1.0	30×25	3C 434.1		

3. The wind-blown effect on the CSB

The five most massive stars in Cyg OB2 are probably responsible for nearly all of the observed wind luminosity. Observations of Cyg OB2 by Abbott et al. (1981) resulted in values of $L_{\rm w} \simeq 5.3\ 10^{38}$ erg s^{-1} and $\rho_0 \simeq 5.85\ 10^{-25}$ g cm^{-3} for the total wind luminosity and the ambient matter density for Cyg OB2.

The radius R and the expansion velocity v of a typical wind blown bubble are expressed in cgs-units as (Castor et al. 1975):

$$R = 0.76 \left(\frac{L_{\rm w}\, t^3}{\rho_0}\right)^{1/5}$$

$$v = 0.46 \left(\frac{L_{\rm w}}{\rho_0\, t^2}\right)^{1/5} \tag{1}$$

where $L_{\rm w}$ is the wind luminosity due to the association which forms the superbubble, ρ_0 is the density of the environment, t is the age of the association. Using Eq. (1), together with the observed luminosity and assuming the CSB is 2 Myr old, Abbott et al. (1981) calculated the radius of the CSB to 175 pc. This result seems to be in agreement with the X–ray observations, especially in view of the large uncertainties of the distance and age of the CSB. Some fine-tuning of the parameters has to be done to match the size of 600 × 450 pc at a distance of 2 kpc.

Difficulties related with this interpretation are

- the assumption of $L_{\rm w}$ to be constant over a period of 2 Myr (Bochkarev & Sitnik 1985);
- the absence of an H I supershell which should be formed by the kinetic energy of 6 10^{51} erg and
- the unresolved background emission of the Cyg X radio source (Abbott et al. 1981).

The regions blown by the wind can be traced by their free-free emission, which radiates in the radio continuum and X–rays outlining the Strömgren spheres. An ordinary O5 star may have a Strömgren sphere as large as 20 pc in radius. Therefore, any correlation of the X–ray structures with large H II regions may provide further hints about the origin of the CSB. For this purpose we have selected H II regions from the Sharpless list with diameters larger than 10′ (listed in Table 2). The observed $V_{\rm LSR}$ velocities, where available, are also given. It is not always clear in this complex region whether a Sharpless region is in fact a single physical object or results from a superposition of structures along the line of sight. Hα filaments distributed over a large region and designated as S109 do not constitute a single object (Dickel et al. 1969). Similar problems might exist for other large objects listed in Table 2.

According to Sitnik & Mel'nik (1996) S101 is related to OB3 and S117, S119 and S125 (not listed in Table 2 due to its size of 9′) are associated with OB7.

4. Supernova-initiated bubble

The rate of SNe plays an important role for the formation of a superbubble. However, the number of known supernova remnants (SNR), which might be physically related to the CSB, is small.

Some of them are too close to us (i.e. Cygnus Loop, HB21, W63), some are outside the field (i.e. G65.7+1.2, G65.3+5.7, CTB87) or too distant (i.e. CTB87, G76.9+1, G84.2−0.8, DA530) to be part of the CSB. Among the remaining SNRs listed in Table 3 about 5 of them are comparable or smaller than the 12′ sampling of the ROSAT all–sky survey maps.

The Cygnus region has been analyzed in detail on both small and large scales for non–thermal sources (Wendker 1970; Wendker et al. 1991). No new non–thermal source could be found. Furthermore, del Rio et al. (1996) analyzed the COMPTEL 1.8 MeV data towards the Cygnus region. Since ^{26}Al, the radioactive decay of which produces the 1.8 MeV line, is a very good tracer of nucleosynthesis and SN, it should be possible to trace both the hidden WR stars and SNRs. They found no evidence of new WR stars and SNRs, which might contribute to the energy content of the CSB.

If ∼10 SNRs are physically related to the CSB and if they are on average visible for about 10^5 yr, then the SN rate within the CSB is one in 10^4 years. Within a period of 2 10^6 yr, the estimated age of the CSB, about 200 SNe would have occurred. This is less than the required 1000 SN explosions (see Sect. 2). However, the lifetime of SNRs

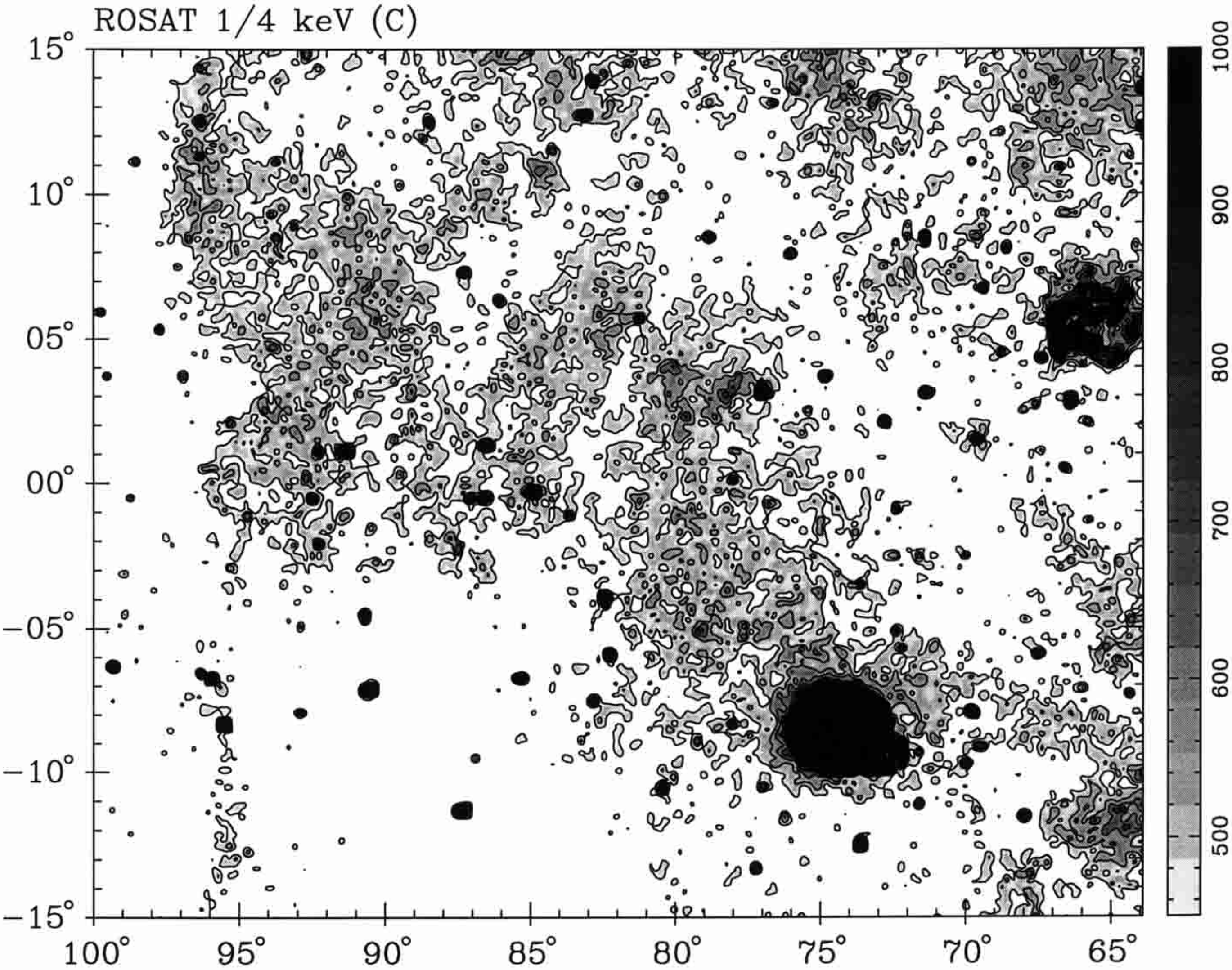

Fig. 2. The region of the Cygnus superbubble as seen in the ROSAT 1/4 keV data. The wedge shows the correspondence between grey scale level and surface brightness units of counts s^{-1} $arcmin^{-2}$. Contours start from 450 counts s^{-1} $arcmin^{-2}$ and are plotted in 100 counts s^{-1} $arcmin^{-2}$ steps. The two high intensity regions are the SNRs G65.1+0.6 and the Cygnus Loop. The extended emission belt running from upper left to lower right is not correlated with the Cygnus superbubble. This emission should be rather local, otherwise it would be absorbed by the H I and CO gas of the so called Great Rift. See text for details

shortens in a dense medium and a higher rate results, although young SNRs are missing in this region.

We conclude that the SNRs located in the region certainly contribute to the X–ray emission, but they are probably not numerous enough to have created the CSB.

5. Observational data

5.1. X–ray observations

The X–ray observations of the CSB have been carried out during the ROSAT all–sky survey. For this paper the surface brightness maps rastered in a $12' \times 12'$ grid have been used. The mean angular resolution during the survey was $\sim 2'$ (HPBW). Maps of different energy bands (cf. Table 4) have been created, covering the range from 0.11 keV to 2.04 keV, or channel 11 to channel 201 of the PSPC pulse height range.

Table 4. The energy bands of the PSPC and corresponding pulse height channels. The fourth column shows the required column density in order to reach the unit optical thickness at the corresponding band.

Band	Channels	Energy (keV)	$N_{\rm H}(\tau = 1)$ 10^{20} $\rm cm^{-2}$
1/4 keV (C)	11–41	0.11–0.28	0.8–1.5
3/4 keV (M)	52–90	0.44–1.21	6.0–15.0
1.5 keV (H)	91–201	0.73–2.04	18.0–60.0

The ROSAT mission is described by Trümper (1983). Details of the X–ray telescope (XRT) are given by Aschenbach (1988) and the PSPC is described by Pfeffermann et al. (1987). Background contamination, scattered solar X–rays, long term background

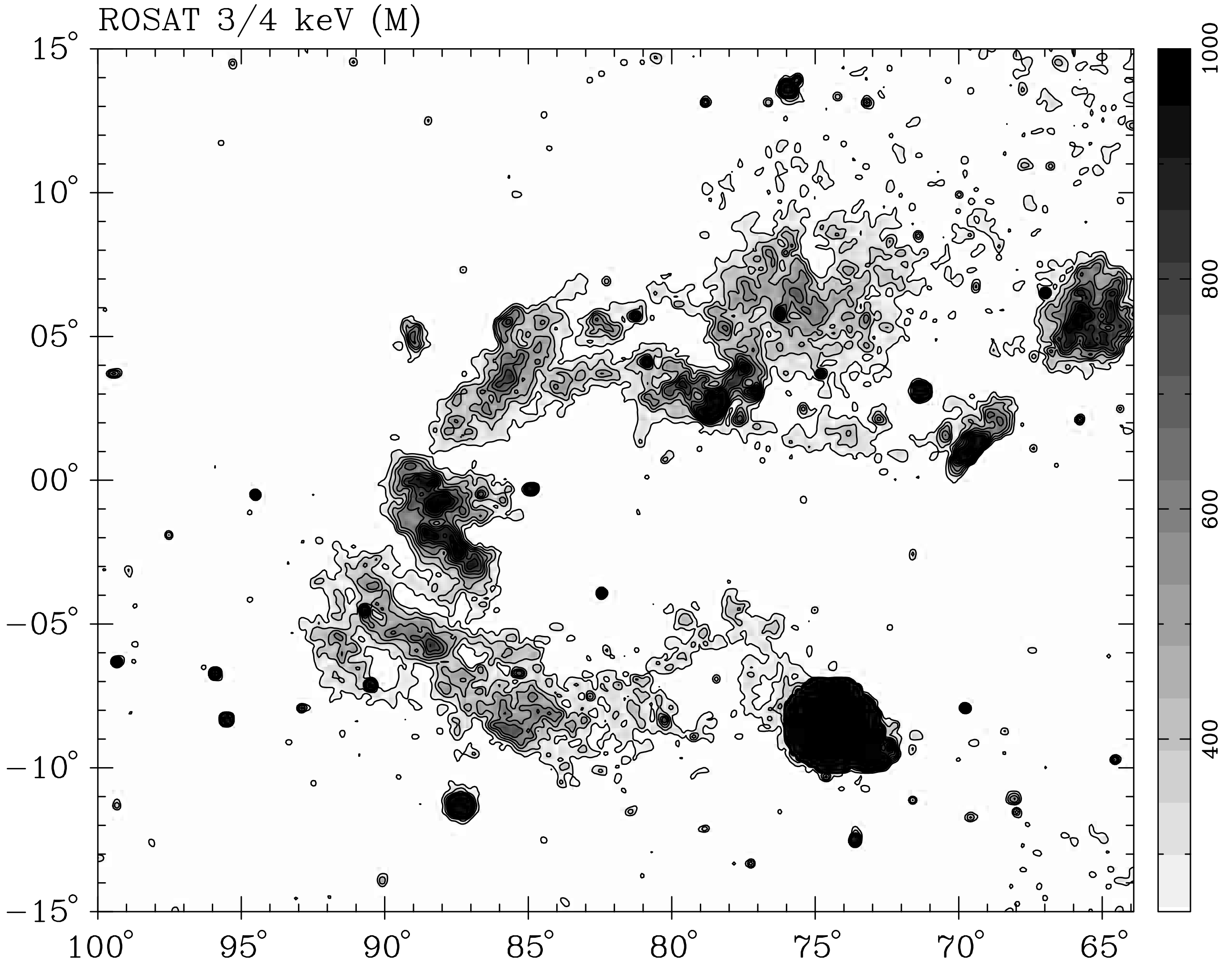

Fig. 3. The Cygnus superbubble as seen in the ROSAT 3/4 keV data. The wedge shows the correspondence between grey scale level and surface brightness units of counts s^{-1} $arcmin^{-2}$. Contours start from 250 counts s^{-1} $arcmin^{-2}$ and are plotted in steps of 100 counts s^{-1} $arcmin^{-2}$. No emission corresponding to the belt in the 1/4 keV band (see Fig. 2) is visible. The 3/4 keV emission is shaped like a horse-shoe. Absorption of soft X–rays happens within and west of the horse-shoe structure. The S 117 ($\ell \sim 85°$, $b \sim -1°$) complex is not obscured and should be located in front of the absorbing material

enhancements and particle background have been treated as described by Snowden et al. (1995).

The 1/4 keV image is shown in Fig. 2. Figures 3 and 4 show the 3/4 keV and 1.5 keV images, respectively. In the medium and high energy band the images are dominated by an arc-like structure ranging from ≈70° to ≈90° in Galactic longitude and from ≈−10° to ≈5° in Galactic latitude. This horse-shoe shaped structure is called the CSB. The details of the X–ray images are discussed in Sect. 7.

5.2. Radio continuum and polarization observations

The map of the Cygnus constellation (35° × 30° in size) is obtained by combining the *Effelsberg 1.4 GHz Medium Latitude Survey* observations (Uyanıker 1997; Uyanıker et al. 1999) with the Galactic Plane Survey by Reich et al. (1990). The data have been absolutely calibrated in both total intensity (using Reich 1982 and Reich & Reich 1986 data) and linear polarization (using data from Brouw & Spoelstra 1976). Details of the *Effelsberg 1.4 GHz Medium Latitude Survey* and data processing are given by Uyanıker et al. (1999, 1998). The total intensity map is shown in Fig. 5, after separating the large scale diffuse background emission. Decomposition of the map into small and large-scale components is based on an unsharp-masking technique (Sofue & Reich 1979).

No linear polarization data are yet available for the Galactic plane but we show the linearly polarized emission for the areas above and below 4° latitude in Fig. 6, after having removed the large scale emission.

5.3. H I data

In the following we make use of the survey of H I emission (Hartmann & Burton 1997), carried out with the

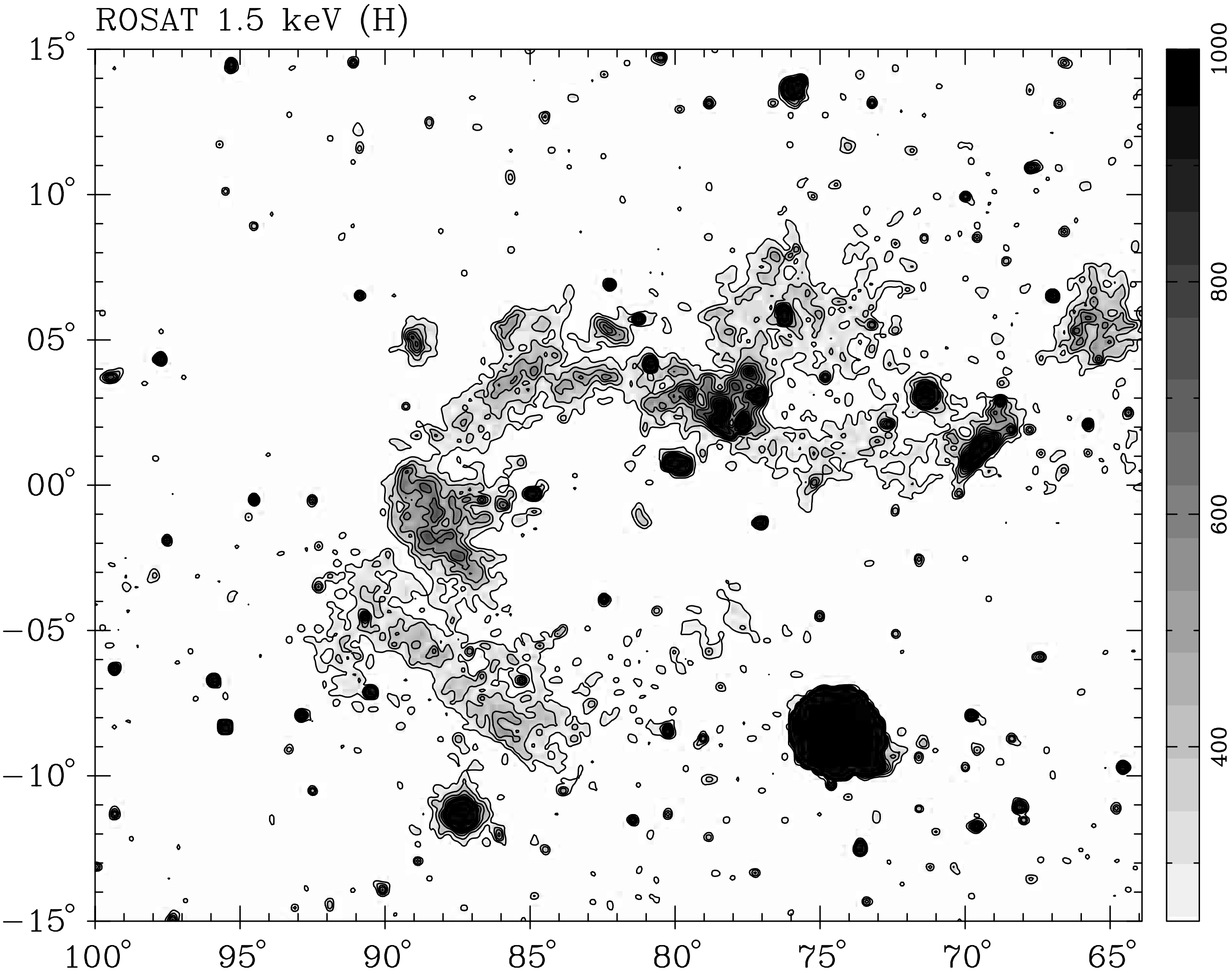

Fig. 4. The Cygnus superbubble as seen in the ROSAT 1.5 keV data. The wedge shows the correspondence between grey scale level and surface brightness units of counts s^{-1} arcmin^{-2}. Contours start from 250 counts s^{-1} arcmin^{-2} and are plotted in steps of 100 counts s^{-1} arcmin^{-2}, same as the 3/4 keV image. The horse-shoe shape can be recognized, but the structures above and below the S117 complex are weaker in comparison to the 3/4 keV image. Furthermore, the part of the southern arc between $\ell = 76°$ and $\ell = 84°$ disappears in this energy range. A comparison of the intensity distributions at 3/4 keV and 1.5 keV indicates that the structures have different spectra (see text)

Dwingeloo telescope for the northern hemisphere. The resolution of this survey is about 36′. We prepared column density maps by integrating the Leiden/Dwingeloo survey spectra in the −300 to 300 km s^{-1} interval. All channel maps have been checked for possible shell and bubble-like structures and these data also serve to find any possible coincidence of the H I structures with those seen at other wavelengths. Figures 7 and 8 show these channel maps at different velocity intervals.

5.4. Infrared data

The Cygnus region consists, with a very few exceptions, of thermal sources (Wendker et al. 1991). Therefore, a close relation to the infrared emission, for example at 60 μm (Fürst et al. 1987), is expected. These authors report a ratio R of the surface brightness of H II regions in the infrared to that at 2.7 GHz of several 100, while for SNRs R is below 10. The latter value may be even smaller at a frequency of 1.4 GHz, because of the higher radio flux density. The IRAS data (Beichmann et al. 1985) in the 60 μm and 100 μm bands show that this emission is well correlated with the radio structures. The infrared data also show the morphology of the dust emission: the dust and the H II continuum are well correlated. Additional information is obtained from the 60 μm/100 μm ratio image in Fig. 9. This image is proportional to the temperature variations of the dust and may be called a color or temperature map. The dust temperature has been obtained using the equation of Young et al. (1995)

$$T_{\text{dust}}(K) = 49 \left(\frac{S_{60}}{S_{100}}\right)^{0.4} . \qquad (2)$$

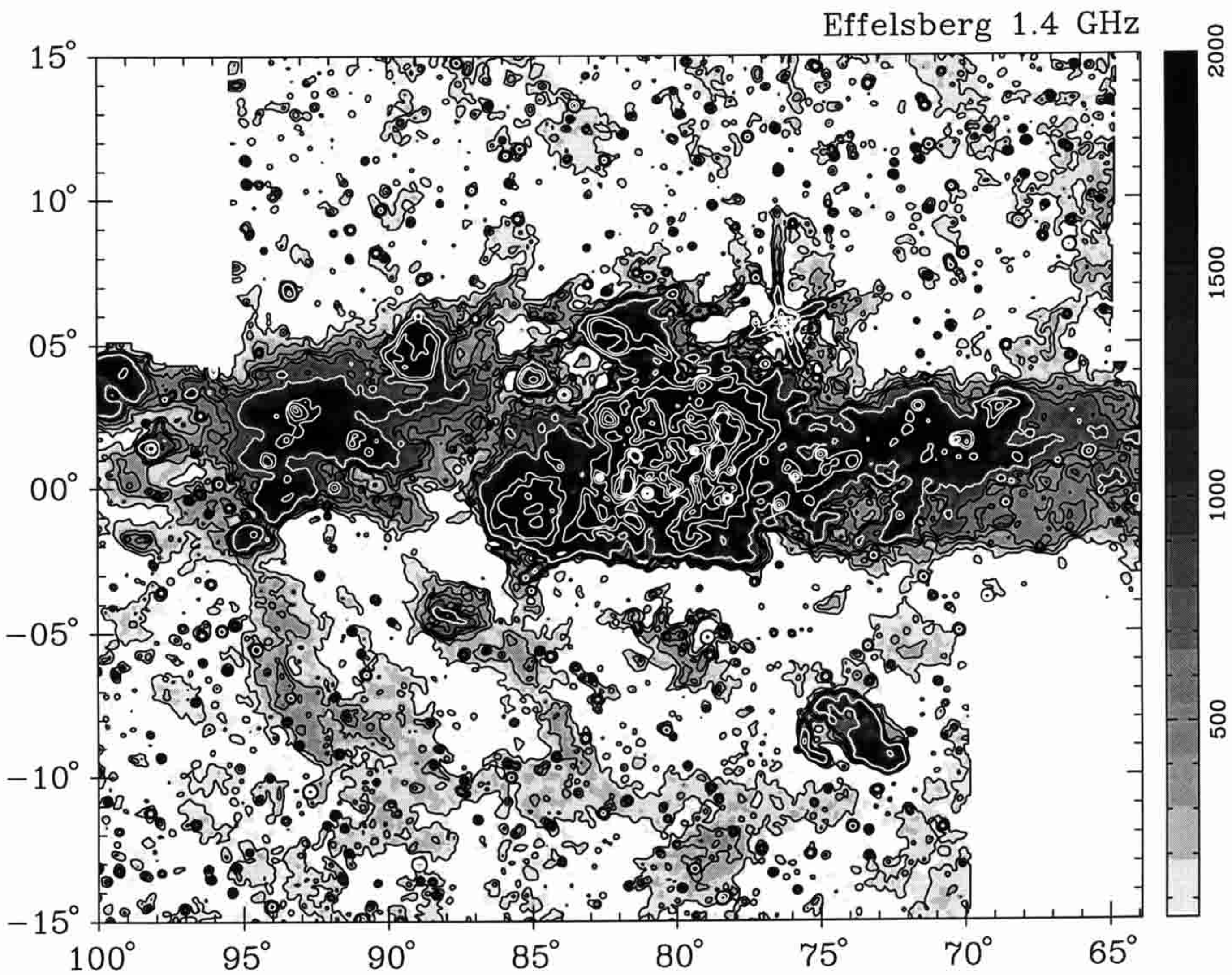

Fig. 5. The Cygnus superbubble region from the new Effelsberg survey at 1.4 GHz. The far sidelobe pattern of the telescope can be seen in the region around Cyg A ($\ell \sim 76°, b \sim 5°$). The first contour set (black contours) starts at 100 mK T_B and runs in steps of 150 mK T_B. The second contour set (white contours) starts at 1000 mK T_B and runs in steps of 1500 mK T_B. The last contour set (also white) is plotted starting at 4000 mK T_B and runs in steps of 4000 mK T_B. The original map has been convolved to a resolution of $12'$

The infrared ratio image (Fig. 9) shows a large elliptical structure centered at $\ell \sim 84\overset{\circ}{.}5$, $b \sim 0\overset{\circ}{.}4$. The major axis of the ellipse fitting this structure is about 25°. The southern part of the ellipse is incomplete, probably due to missing IRAS data of that region. Nevertheless, the south–east portion of the 60 μm/100 μm image envelopes the X–ray emission and the variation of the dust temperature across the whole elliptical structure is evident. For example the dust temperature, inferred from Eq. (2), is about 25 K in the south–east, whereas it is about 37 K towards Cyg–X region.

The temperature sensitive map (Fig. 9) also shows the bubble probably associated with the OB1 ossociation (Lozinskaya & Repin 1990), at $\ell \sim 75°$, $b \sim +1°$.

As in the other wavelengths, infrared emission shows bubble-like structures. Some of these structures are possibly related with the shells or bubbles in other wavelengths and some do not even coincide positionally. This appearance and complexity of the region makes it difficult to resolve the individual structures at different wavelengths as well as the possible relationship between them.

5.5. CO data

The molecular content of the Cygnus region has been investigated using the CO survey at 115 GHz (the $J = 1 - 0$ rotational transition) of Dame et al. (1987). The channel width of these data is 1.3 km s^{-1}. The data have been searched for CO emission from -100 to 100 km s^{-1}. Discrete CO structures have been found between -12 km s^{-1} and $+18$ km s^{-1} (see Fig. 10). For the figure, four channel maps have been integrated.

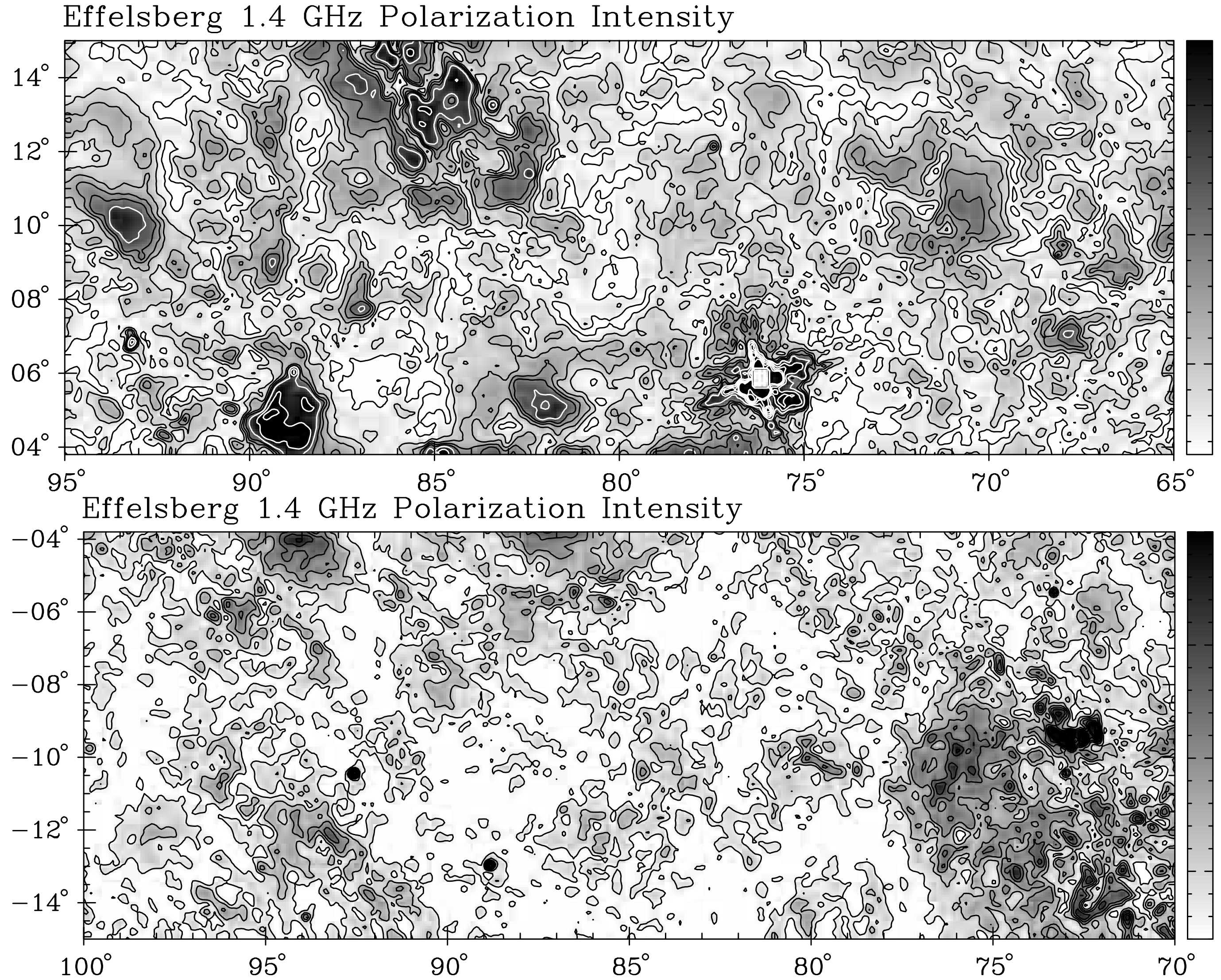

Fig. 6. The polarized intensity maps of the Cygnus superbubble region from the Effelsberg Medium Latitude Survey at 1.4 GHz. The two panels show the northern and the southern part of the Cygnus region, respectively. A smooth background has been subtracted from the U and Q data in order to enhance the small scale structures as described in Sect. 6.1. For the upper panel contours start at 30 mK $T_{\rm B}$ and run in steps of 40 mK $T_{\rm B}$ in black and in white from 250 mK $T_{\rm B}$ in steps of 100 mK $T_{\rm B}$. For the lower panel contours start at 30 mK $T_{\rm B}$ and run in steps of 30 mK $T_{\rm B}$. The maps are convolved to 12′ angular resolution

6. Radio structures towards the CSB

In the total intensity radio map of the Cygnus region (cf. Fig. 5) no structures show up which resemble the horse–shoe shaped X–ray structure. The projection of numerous SNRs, H II regions and various radio structures form a complicated picture. The distribution of these objects is very irregular, giving the impression that their arrangement is accidental along the spiral arm. Where the CSB intersects the Galactic plane (at $\ell \sim 88°$) the radio continuum emission reaches a local minimum. West of this local minimum several well-known objects are located: the Cygnus X region (highest intensity region towards $\ell = 78°$, $b = 2°$, including DR4), S 117 (North America nebula $\ell = 86°$, $b = -0\overset{\circ}{.}5$) and IC 5067 (Pelican nebula $\ell = 84\overset{\circ}{.}5$, $b = 0\overset{\circ}{.}0$). East of the local minimum several other emission complexes such as HB21, DA530 are located.

The thermal filaments close to the SNR W63 ($\ell = 82\overset{\circ}{.}2$, $b = 5\overset{\circ}{.}3$) showing up in the radio image are also visible in the 60 μm/100 μm infrared ratio image (Fig. 9). According to Eq. (2) the corresponding infrared ratio of ≈0.33 translates to a dust temperature of about 30 K. These filaments depolarize and increase the rotation measure of the polarized radio emission from W63 (Uyanıker et al. in prep.). They are, therefore, in front of the SNR.

W63 and most of the other SNRs in this region do not show up at 60 μm and 100 μm as is expected from the known low ratio of infrared to radio emission for SNRs. An exception is the Cygnus loop, which is clearly visible in the 60 μm/100 μm infrared ratio image. This infrared emission also correlates with the optical emission (Arendt et al. 1992).

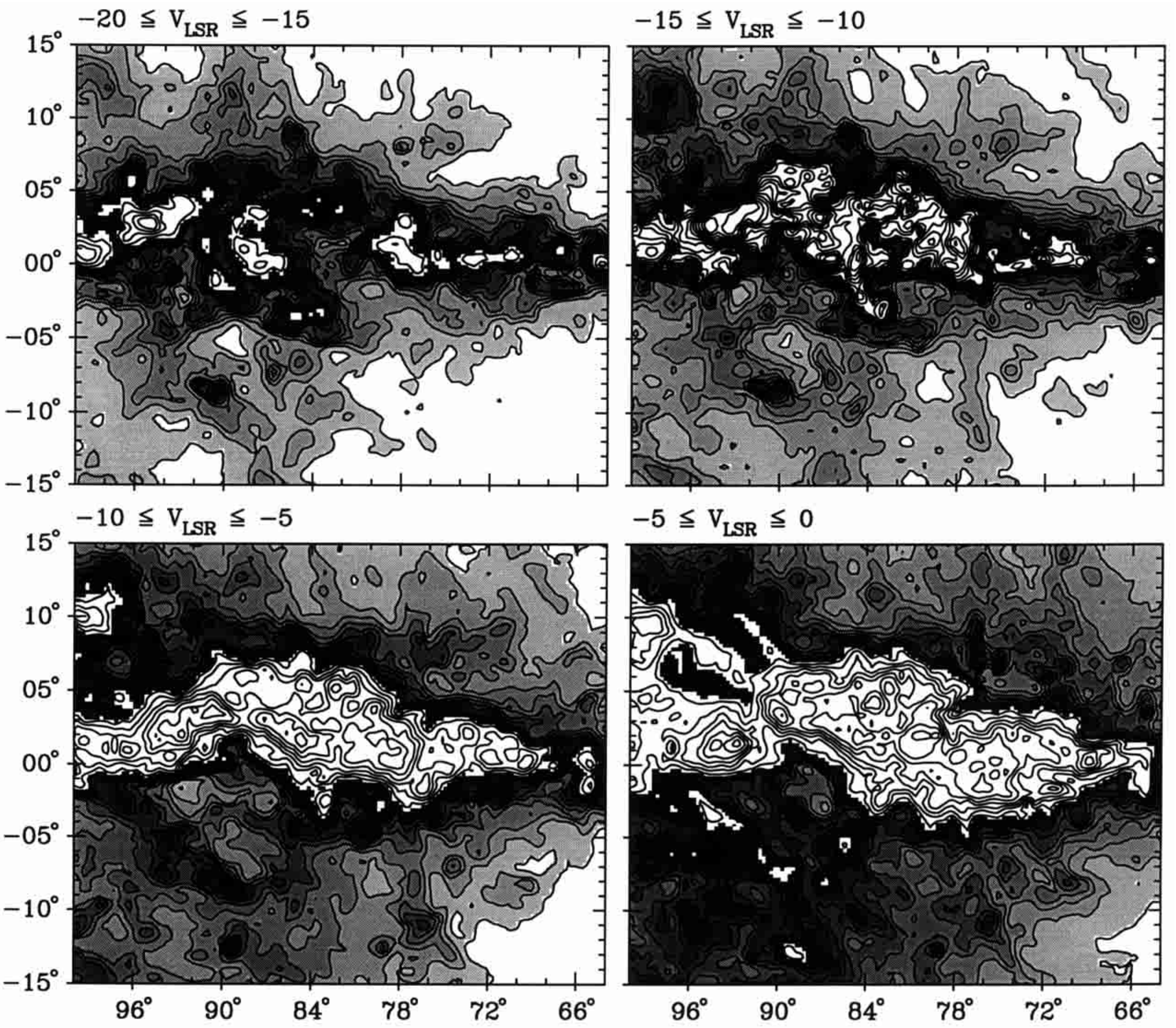

Fig. 7. HI data towards the Cygnus region at different velocity intervals. For all of the panels contours start at 0.5 10^{20} cm^{-2} and run in steps of 0.5 10^{20} cm^{-2} up to 5 10^{20} cm^{-2}, then further in steps of 1 10^{20} cm^{-2}

Apart from SNRs and H II regions, the most prominent, large scale structure outside the Cygnus X complex is the one running from $\ell \sim 96°$ perpendicular to the galactic plane and bending in an arc towards the Cygnus Loop. The size of this arc-like feature is >10° in latitude and 20° in longitude. Another arc joins at $\ell \sim 84°$, apparently originating from H II region S119 ($\ell = 88°$, $b = -4.^{\circ}0$). This second arc has about the same extent in latitude as the previous one. The two arcs are too faint to show up in the 408 MHz survey (Haslam et al. 1982) and the Stockert 1.4 GHz survey (Reich & Reich 1986) because of confusion with the high absolute background emission level.

The southern arc of the CSB is located between these two radio arcs and there exists a clear anticorrelation between radio and X–ray emission in this area (see Fig. 11). The eastern arc structure seen in the total intensity radio map can also be traced in the infrared maps (see Sect. 5.4 and Fig. 9). As mentioned in Sect. 5.4 the ratio R of the surface brightness at 60 μm to that at 1.4 GHz may be used to identify thermal structures. The southern arc has a mean ratio R varying between 0.3 to 2.0 MJy sr^{-1} mK^{-1}, whereas this ratio is 0.02 for HB21, 0.03 for Cygnus Loop and 0.04 for W63. This favors a thermal nature of the structure. In general, our data do not indicate the presence of additional non–thermal sources.

6.1. Polarized emission

We have measured a significant amount of polarized emission at 1.4 GHz in the Cygnus region as shown in Fig. 6. Since we are mainly interested in the more distant structures and their relation to the CSB, we have filtered out the large scale very local emission from the polarized intensity maps. The Stokes U and Q maps are smoothed to an angular resolution of 3° and then subtracted from the original maps, which were observed with a $9.'4$ beam. To increase the signal–to–noise ratio we have convolved the resulting maps to $12'$ angular resolution. Thus a direct comparison of the structures in the radio continuum and X–ray images is possible.

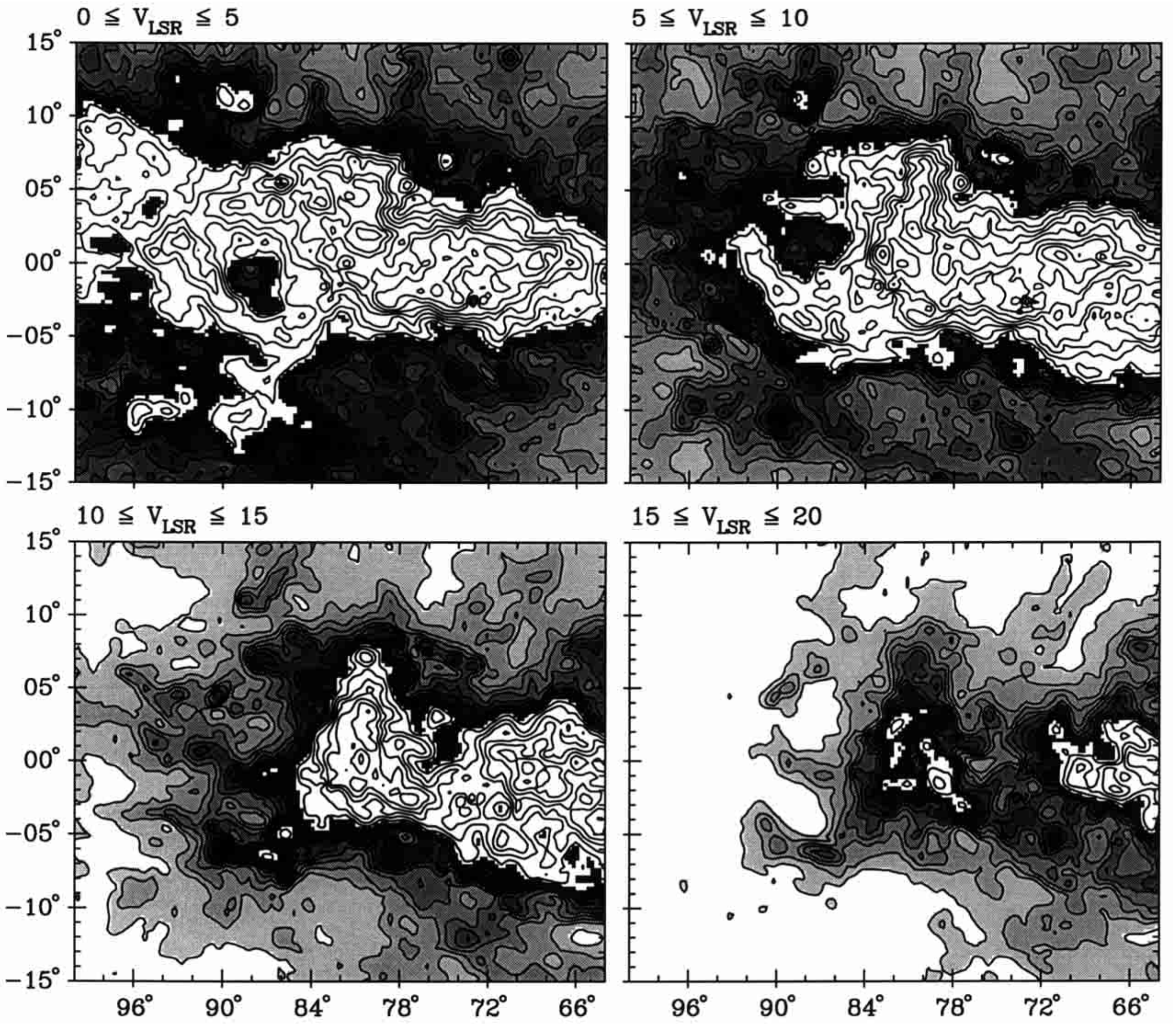

Fig. 8. Same as Fig. 7 but for different velocities

The existence of linear polarization requires non–thermal emission. However, strong thermal emission is known to dominate the Cygnus X region (Wendker et al. 1991). This thermal emission will depolarize the non–thermal emission originating at the same or at larger distances. Due to the Faraday effect the plane of polarization of the linearly polarized radio wave rotates as it passes through a magneto-ionic medium by an amount of

$$\begin{aligned}\Delta\phi[\mathrm{rad}] &= 0.81\ \lambda^2[\mathrm{m}^2] \int_0^L B_{||}[\mu\mathrm{G}]\ n_\mathrm{e}[\mathrm{cm}^{-3}]\ \mathrm{d}s[\mathrm{pc}] \qquad (3)\\ &= \lambda^2[\mathrm{m}^2]\ RM\end{aligned}$$

where n_e is the electron density, s is the distance along the line of sight, $B_{||}$ is the component of the magnetic field along the line of sight, λ is the wavelength and RM is the rotation measure. The sign of RM indicates the direction of the magnetic field. A positive value indicates a field towards the observer. Inhomogeneous media and the finite angular resolution lead to various types of depolarization. In fact, the polarized emission shown in Fig. 6 appears to be patchy, as might result from nonuniform depolarization. There exist several examples of depolarization structures similar to the depolarization filaments discovered in the direction of the Galactic anticenter (see Uyanıker 1997; Uyanıker et al. 1999), the origin of which is not yet clear. In general, there is no correspondence of polarized structures with features in the total intensity map. Exceptions are some SNRs, such as the bright objects W63, HB21 and the Cygnus Loop. However, these structures contribute only a small fraction to the entire polarized emission.

The polarized emission (Fig. 6) also seems to be anticorrelated with the X–ray structure. However, there is evidence for a polarized structure enveloping the thermal southern arc, but not coincident with it.

We should mention that near $\ell = 76°$, $b = 5°$ the polarization map is somewhat affected by the strong signal from the radio galaxy Cyg A.

A few outstanding polarization features are visible, which are not associated with SNRs. They will briefly be discussed in the following sections.

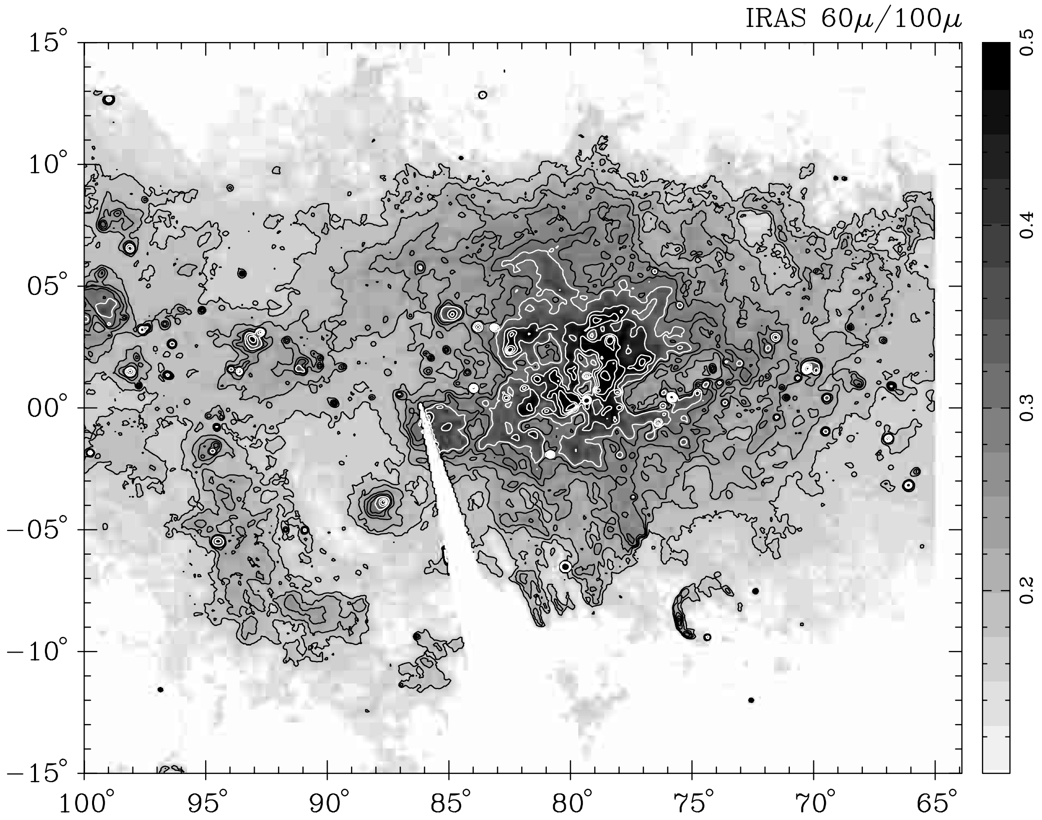

Fig. 9. Infrared 60 μm/100 μm ratio image of the CSB region. The contours start at 0.175 and run in steps of 0.03. The white contours start at 0.325 and run in steps of 0.09. An elliptically shaped structure centered at $\ell \sim 84.^{\circ}5$, $b \sim 0.^{\circ}4$ can be seen. The ellipse fitting the shape of the structure has a major axis about 25° and a minor axis ~16°. The tilt angle is ~30° with respect to the Galactic plane. The grey scale is proportional to the temperature of the dust in terms of lighter (cold) and darker (hot) shadings

6.2. A small section from Loop II and Loop III

Towards $\ell = 85^{\circ}$, $b = 11^{\circ}$ a part of the known radio Loop II can be traced in polarized emission. The Loops II and III overlap near $\ell = 91^{\circ}$ and $b = 12^{\circ}$ (see Fig. 1). Several depolarization structures are seen in that direction. The loops are non–thermal, polarized, local structures with distances of about 175 pc for Loop II and 200 pc for Loop III (Berkhuijsen 1973). These distances mark also the upper limit for the distance of the depolarization filaments.

If these depolarization structures were behind the radio loops, then the superposed polarized emission from the loops would scramble the polarization of the filaments. The rotation measure in this area, derived from the compilation of Dwingeloo data by Brouw & Spoelstra (1976), changes between 3 to 7 rad m^{-2}. For an interstellar magnetic field of 3 μG and a density of thermal electrons of 0.01 cm^{-3} the distance is ≈100 pc. All these structures are, therefore, very local.

6.3. Polarization structure at G93.9+11.6

In the northern Cygnus region there exists a distinct emission feature at $\ell = 93.^{\circ}9$, $b = 11.^{\circ}6$. It is about $2.^{\circ}5 \times 4.^{\circ}5$ in size, along ℓ and b, respectively. Although the peak polarization at about $\ell = 93.^{\circ}12$ and $b = 10.^{\circ}15$ is due to a polarized compact source, most of the structure – with a possible exception of the northern arc – cannot be attributed to a discrete continuum source. There is very faint continuum emission (at a level not visible in Fig. 5) at the position of the northern arc (see Uyanıker et al. 1999).

Neither the 60 μm and 100 μm IRAS data nor the ROSAT survey data show any features associated with the polarized emission nor with the total-power emission from the northern arc. The percentage polarization of the enhancement is ~9%, whereas the loop in the north has a percentage polarization ~6%, calculated with respect to the total intensity background, where the 2.8 K cosmic background component has been subtracted.

The observed large size of the structure indicates that it might be local. The coherent polarization structure might indicate small fluctuations of the local magnetic field in this direction.

6.4. Southern part

The southern part of the Cygnus region shows different properties in comparison to the northern part as there are several large scale polarization structures between $\ell \sim 75^{\circ}$ to $\ell \sim 95^{\circ}$ as mentioned above.

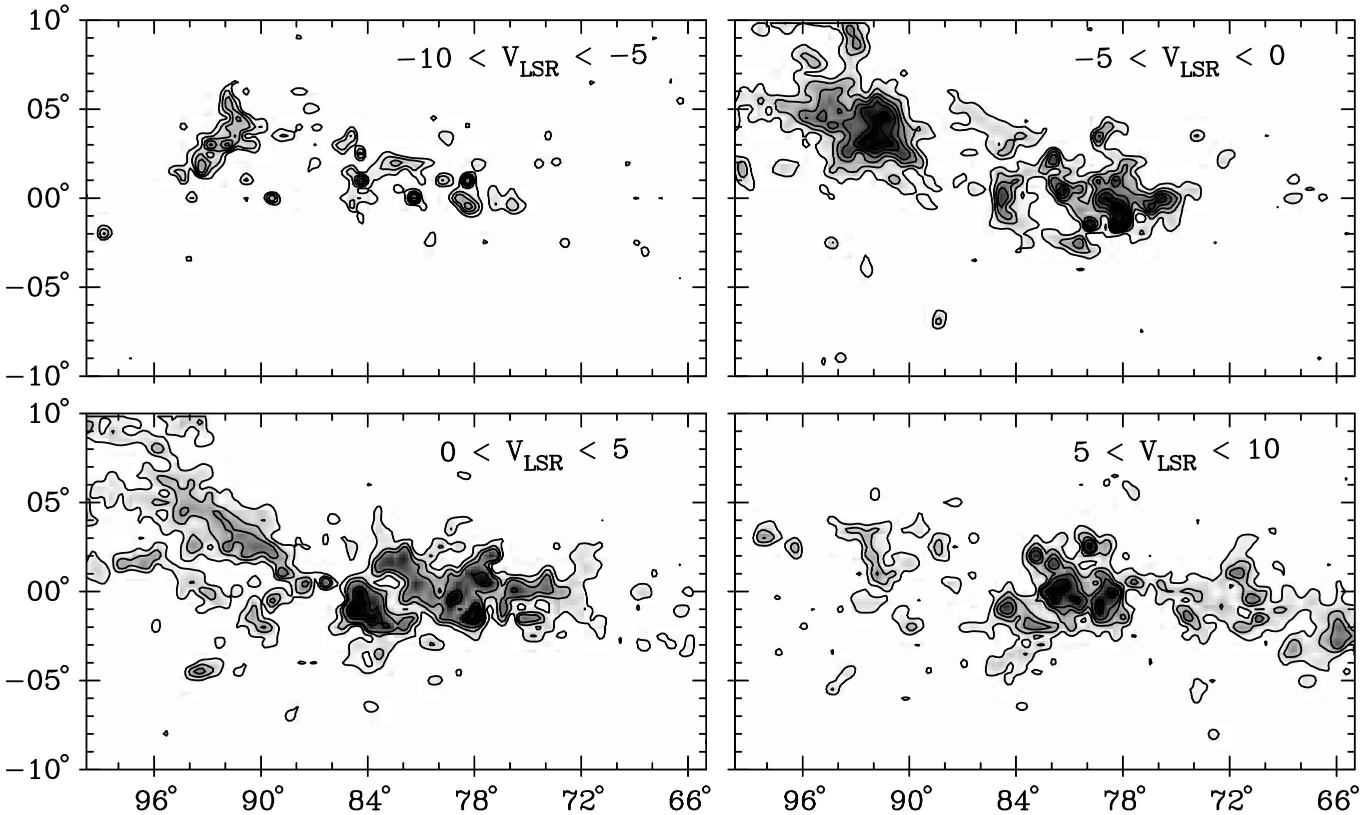

Fig. 10. CO data of the Cygnus region at different velocity intervals. The contours start from 1500 mK and run in steps of 1000 mK for the upper left panel. For the other panels the steps are 2000 mK. This figure demonstrates the kinematical differences of the molecular gas in the field. The absorbing gas consists of two kinematically distinct major groups located east and west of $\ell \sim 86°$

Another structure is a large patch of emission south of the Cygnus Loop. The structure has no sharp boundaries but it covers an area of at least $6° \times 6°$. No prominent total-power emission associated with the polarized structure is seen.

7. X–ray structures

Since the work by Bowyer et al. (1968) the anticorrelation between the soft X–ray intensity and the Galactic neutral hydrogen distribution is known. At 1/4 keV the optical depth $\tau = 1$ is reached for a neutral gas column density of 1.5 10^{20} cm^{-2}. All detected emission at this energy originates within a distance of $\lesssim$300 pc. Emission arising at larger distances is absorbed. The emission at soft X–ray energies (0.1–0.5 keV) is dominated by the hot gas surrounding the Sun, the "Local Hot Bubble" (see the review by McCammon & Sanders 1990), which is ~100 pc in size and has a temperature ~10^6 K.

At 3/4 keV and 1.5 keV an optical depth of unity is reached for a path length in the disc of about 1 kpc ($N_{\rm H\,I} \approx 1.2\ 10^{21}$ cm^{-2}) and 5 kpc ($N_{\rm H\,I} \approx 1.1\ 10^{22}$ cm^{-2}), respectively (e.g., Rosen et al. 1996; Morrison & McCammon 1983).

7.1. ROSAT 1/4 keV data

The 1/4 keV image of the CSB region is shown in Fig. 2. This emission should be local and probably closer than the CSB. The most prominent features in this map are the two bright and nearby SNRs, the Cygnus Loop and G65.2+5.2. A large diffuse emission structure extends from the Cygnus Loop in the north–east direction. This emission belt can not be seen in the higher energy X–ray images. Some emission from the northern part of the 1/4 keV image coincides spatially with the CSB. Most of the coincidental 1/4 and 3/4 keV emission is seen in the region where DR4 (Cyg X) ($\ell = 78.2$ and $b = 2.1$) is located, which consists of objects unrelated to the CSB projected along the line of sight (see Dickel & Wendker 1978). No such coincidence is seen in the southern part. This indicates that the X–ray spectrum across the CSB is not uniform. Since the ROSAT bands are not completely independent from each other because of the spectral overlapping the association of at least some structure in the 1/4 keV maps with more distant sources might be real.

7.2. ROSAT 3/4 and 1.5 keV data

The shape of the CSB can be recognized much more clearly in the 3/4 keV and 1.5 keV data (Figs. 3 and 4). The X–ray emitting loop-like structure has dimensions of

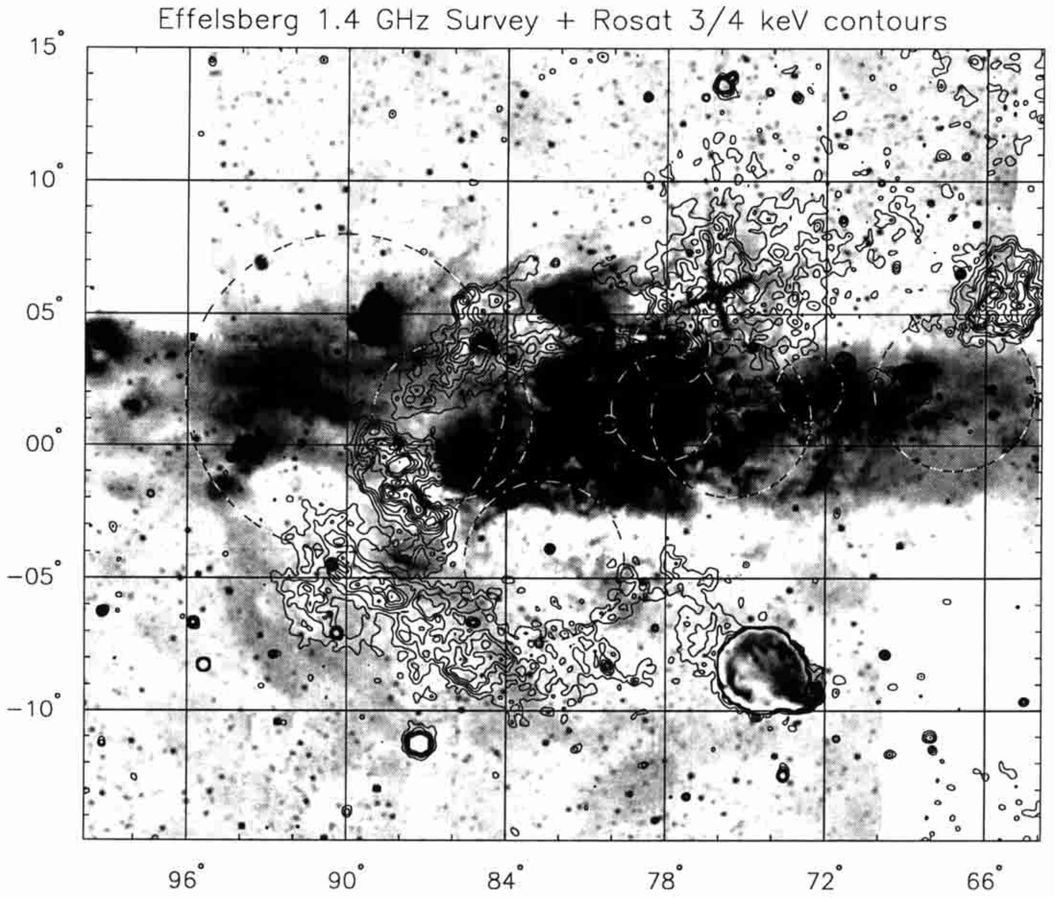

Fig. 11. The Cygnus region from the 1.4 GHz survey shown in gray scale and the ROSAT 3/4 keV data superposed by contours. Circles show the approximate positions and extents of OB associations

at least 18° × 14° in ℓ and b, which is slightly larger than previously quoted by Cash et al. (1980). In these energy bands there is a pronounced reduction in surface brightness shaped like a belt extending along $\ell \sim 65°$ to $100°$ starting at $b \sim -10°$ and passing across the CSB and reaching up to $b \sim +10°$. This belt also covers the Great Rift (also called the Cygnus Rift, Pyne 1960; Lucke 1978) and is tilted about 30° with respect to the Galactic plane. The Rift is associated with S117 (North-America nebula) and IC 5067 (Pelican nebula), both at a distance of 0.8 kpc according to Brand & Blitz (1993), while Straižys et al. (1989) determined the distance of the S117 complex to be 0.55 ± 0.1 kpc using photometric measurements. The Rift mainly consists of three different molecular clouds at different distances. The western side of the Rift ($\ell \sim 60°$) has a distance of about 1.6 to 2 kpc (Miller 1937; Uranova 1968) and the eastern side ($\ell \sim 90°$) is at a distance of 0.5 to 0.8 kpc (see Uranova 1968; Lucke 1978).

The variations of the flux in the 3/4 and 1.5 keV energy bands can be used to study in more detail the origin of the CSB. For that purpose we have prepared hardness ratio images of the region as follows

$$HR_1 = \frac{M-C}{C+M} \qquad (4)$$
$$HR_2 = \frac{H-M}{M+H}$$

where C, M and H are the 1/4, 3/4 and 1.5 keV data, respectively. A small value of the ratio, thus, indicates a soft spectrum whereas a high value represents a hard spectrum.

The HR_1 hardness ratio map presented in Fig. 12 shows some variations. For values $HR_1 \gtrsim 0.2$ a significant portion of the southern arc is not visible. The portions of the hardness ratio map corresponding to very soft spectra positionally coincides with the Cygnus Rift (diagonally extending white area in the map). This supports the idea that the view of the region in general is due in large part to the absorption of X–rays by foreground material. From the remaining emission structures the horse-shoe shaped CSB can hardly be recognized. Therefore a detailed analysis is needed. For a more quantitative analysis we have selected rectangular areas across the CSB for which the hardness ratio distribution of some prominent regions has been calculated. Areas of $28' \times 28'$ in size are found to represent the structures quite well and provide enough count statistics. The selected areas in the individual structures are shown in Fig. 13. The mean HR value within each box-area is determined and plotted against box number in Fig. 14. The HI column densities corresponding to the same box are also determined and plotted in Fig. 14. Furthermore, the same method is applied to the 60 μm and 100 μm IRAS

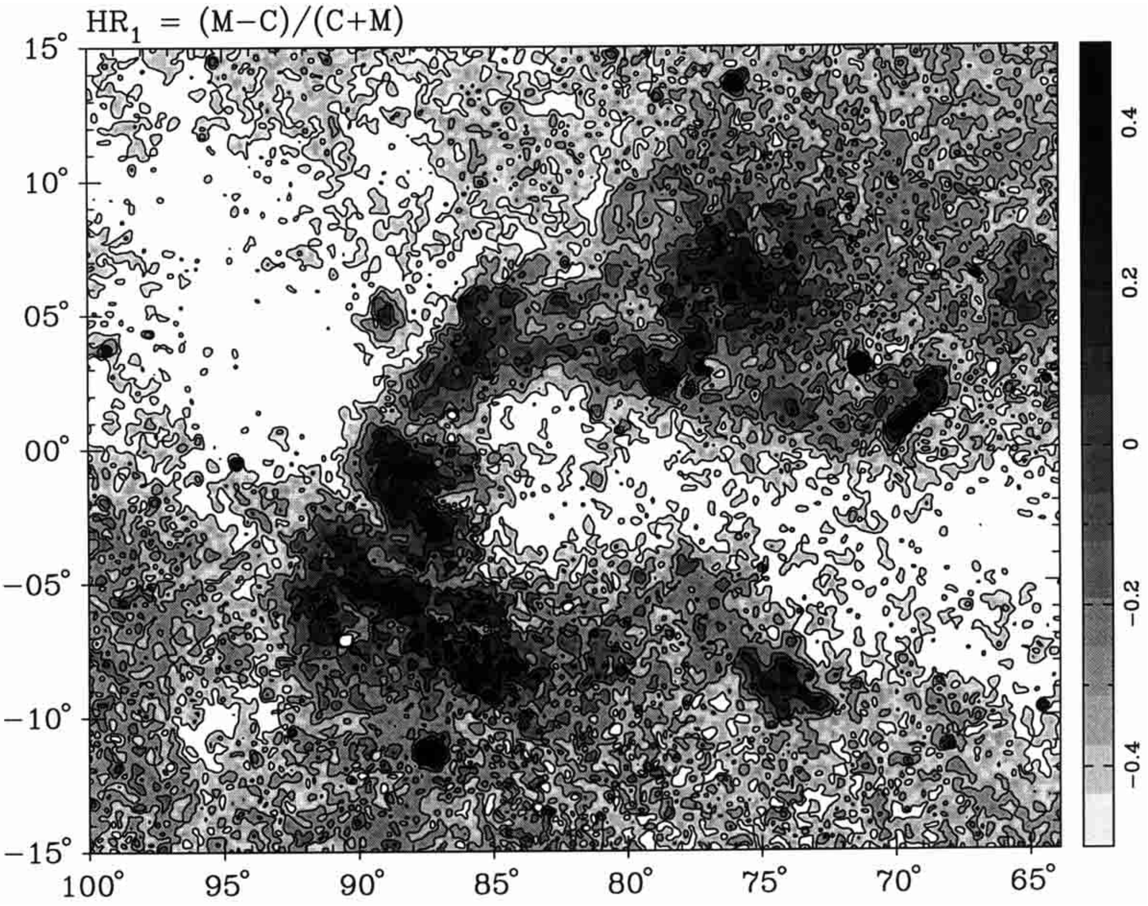

Fig. 12. Hardness ratio image HR_1 of the CSB. Contours start at −0.6 and run in steps of 0.2

images and to their ratios giving the variation of the color temperature along with the X–ray structures (see Fig. 14).

Another way of obtaining the temperature variations in the PSPC survey maps has been introduced by Snowden et al. (1997). They have modeled the expected X–ray intensities for the PSPC instrument for a hot plasma model (Raymond & Smith 1977) as a function of the absorbing hydrogen column density. Thus, expanding the work of McCammon et al. (1983), for the Wisconsin survey, they have shown that the band ratio images provide information on the temperature and the location of the emitting material. Following this work, we have prepared the $R2/R1$ (PSPC channels 20–41/11–19 = upper to lower half of C band) and $R5/R4$ (PSPC channels 70–90/52–69 = upper to lower half of M band) band ratio images of the Cygnus region and expanded our analysis by applying the box technique we have used for the other images. Furthermore, the intensities from the C, M and H bands and from the CO map are extracted in the same way. The resulting plots are displayed in Fig. 15. For a typical region near the Galactic plane the ratio of the molecular hydrogen column density to the ^{12}CO line intensity

$$\chi = N_{\mathrm{H}_2}/W(^{12}\mathrm{CO}) \tag{5}$$

is between 1.6 10^{20} and 2.3 10^{20} (K km s^{-1})$^{-1}$ (Strong et al. 1988; Bloemen et al. 1990).

7.3. Analysis of individual regions

The observed X–ray emission from an object depends on its distance, the absorbing material along the line of sight and the intrinsic spectrum of the source. Therefore, a comparison of the emission and absorption characteristics of the individual fields provides further hints about the distance and origin of the observed structures. In this section we compare the results obtained from different maps based on the box-method for each region. Most of the information is obtained from the comparison of the hardness ratio and the H I column density. Figure 14 shows that the column density is very different for the various boxes. We have estimated the H I column density integrated between various intervals of radial velocity (Fig. 16). Towards the CSB there is still a distance ambiguity for positive radial velocities. H I gas at radial velocities <−30 km s^{-1} is located at distances larger than 5 kpc.

G65 (box-no. 1–19): The hardness ratios towards this object indicate a systematic decrease of the X–ray intensity with increasing energy ($C > M > H$, see Fig. 15). For radial velocities between 0 and 15 km s^{-1} (distance 0–1 kpc) the H I of $N_{\mathrm{H\,I}} \simeq 8\ 10^{20}$ cm^{-2} indicates low absorption of the X–ray bands. Because of the distance ambiguity part of this gas may be located at much larger distances. Most of the H I is located at distances beyond

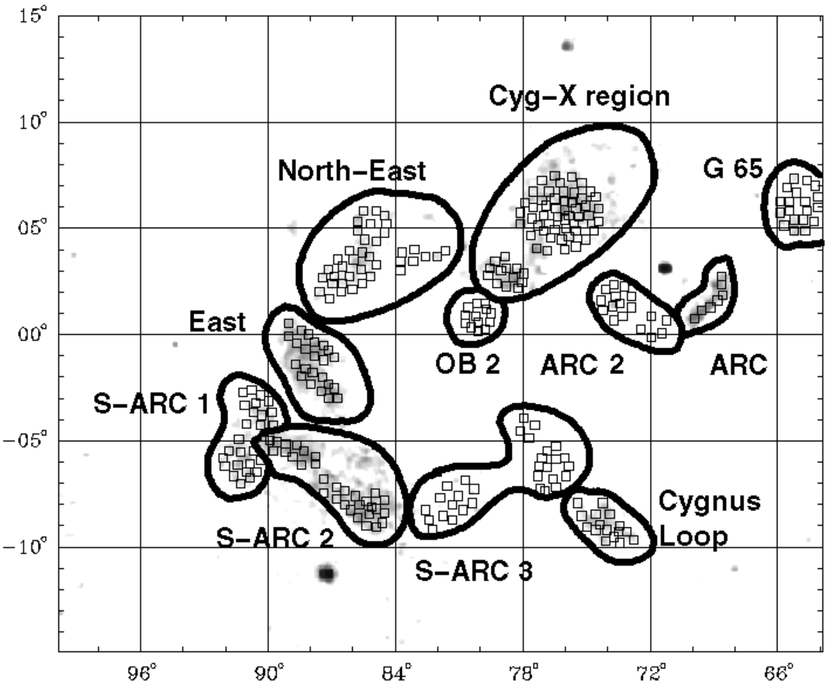

Fig. 13. The sketch of positions selected to study the variations in the observed emission. Boxes of $28' \times 28'$, from the individual regions of the CSB named in the figure, are used to extract intensities from maps at different wavelengths

G65 (see Table 3). This is in agreement with the systematic decrease of the X–ray emission over the various bands.

ARC (box-no. 20–26), ARC-2 (box-no. 27–43): Towards both structures high absorbing material ($N_{\rm H\,I} \simeq 9\ 10^{21}$ cm^{-2} and $N_{\rm H_2}$ up to $\simeq 2\ 10^{21}$ cm^{-2}) is detected. The hardness ratio HR_2 is very similar for both arcs. They differ with respect to HR_1, which is high for ARC (low C band emission) and low for ARC-2 (high C band emission compared to to M band). If the emission in the different X–ray bands is physically related to the same object (in particular for ARC-2), ARC should be at a larger distance than ARC-2.

Cyg-X (box-no. 44–108): $N_{\rm H\,I}$ value changes between (1.5–10.0) 10^{21} cm^{-2} and $N_{\rm H_2} \simeq 0.2\ 10^{21}$ cm^{-2}. There is less C band but relatively high M and H band emission. The spectrum is hard and consists of at least two components. The south-east part of the source has similar hardness ratios as the north-west part, but the column density is about a factor 4 larger. Most of this material is at large distances (radial velocity <-40 km s^{-1}). The increase in column density does not affect the hardness ratios. Therefore, the Cyg–X region is probably at a distance <5 kpc. A low distance is necessary at least for the south-east part of the object. We observe high infrared emission from this region and the infrared ratio map indicates a dust temperature of about 37 K.

North-East: (box-no. 109–146) In this region $HR_1 > 0 > HR_2$. The soft emission at the C and M bands can easily be blocked by the high absorbing material ($N_{\rm H\,I} \simeq 8\ 10^{21}$ cm^{-2}). This field contains HB21 and W63. Molecular gas (column density $N_{\rm H_2} \simeq 0.8\ 10^{21}$ cm^{-2}) is high enough to obscure the whole C band and some part of the M band emission. The high value HR_1 indicates that some of the soft emission is absorbed. On the other hand, the M band emission is still strong ($HR_2 < 0$). Since the H I column density is high enough to absorb most of the M band emission, the corresponding X–ray gas should be closer than the majority of the H I gas, probably closer than a few kpc. SNR HB21 interacts with molecular gas, which belongs to the Cyg OB7 association (Tatematsu et al. 1980). Thus, HB21, the molecular gas and OB7 have the same distance, i.e. ∼800 pc see also Tables 1 and 3).

East: (box-no. 147–169) This region, towards the S 117 complex, contains molecular gas ($N_{\rm H_2} \simeq 0.6\ 10^{21}$ cm^{-2}) and a large amount of neutral gas ($N_{\rm H\,I} \simeq 3\ 10^{21}$ cm^{-2}). The hardness ratio indicates a hard spectrum in the soft energy bands ($HR_1 > 0 > HR_2$) but a soft spectrum at higher energies. Compared with the North-East region the C band emission is much more strongly absorbed indicating a larger distance. This is particularly obvious for the southern part of this area. The column density is much lower than for the northern part, but still the C band emission appears much less absorbed than the M band emission.

S-ARC 1 (box-no. 170–195): Across this region we observe a relatively low amount of molecular and neutral gas ($N_{\rm H\,I} \simeq 1.8\ 10^{21}$ cm^{-2} and $N_{\rm H_2} \simeq 0.2\ 10^{21}$ cm^{-2}). The spectrum is soft ($HR_1 \sim 0 > HR_2$) with $C > M > H$. The total column density is large enough to absorb the C band emission significantly. Therefore, the X–ray spectrum suggests a relatively low distance of about 1–3 kpc.

S-ARC 2 (box-no. 196–226): This field is distinct from the S-ARC 1 and S-ARC 3 fields by its harder spectrum ($HR_1 > 0 > HR_2$), although the molecular and atomic column densities of this region are similar to S-ARC 1. The low C band emission compared to M band suggests a larger distance than for S-ARC 1.

S-ARC 3 (box-no. 227–257): This structure differs from the other southern regions by its soft spectrum ($HR_1 < HR_2 < 0$), although there is more absorbing

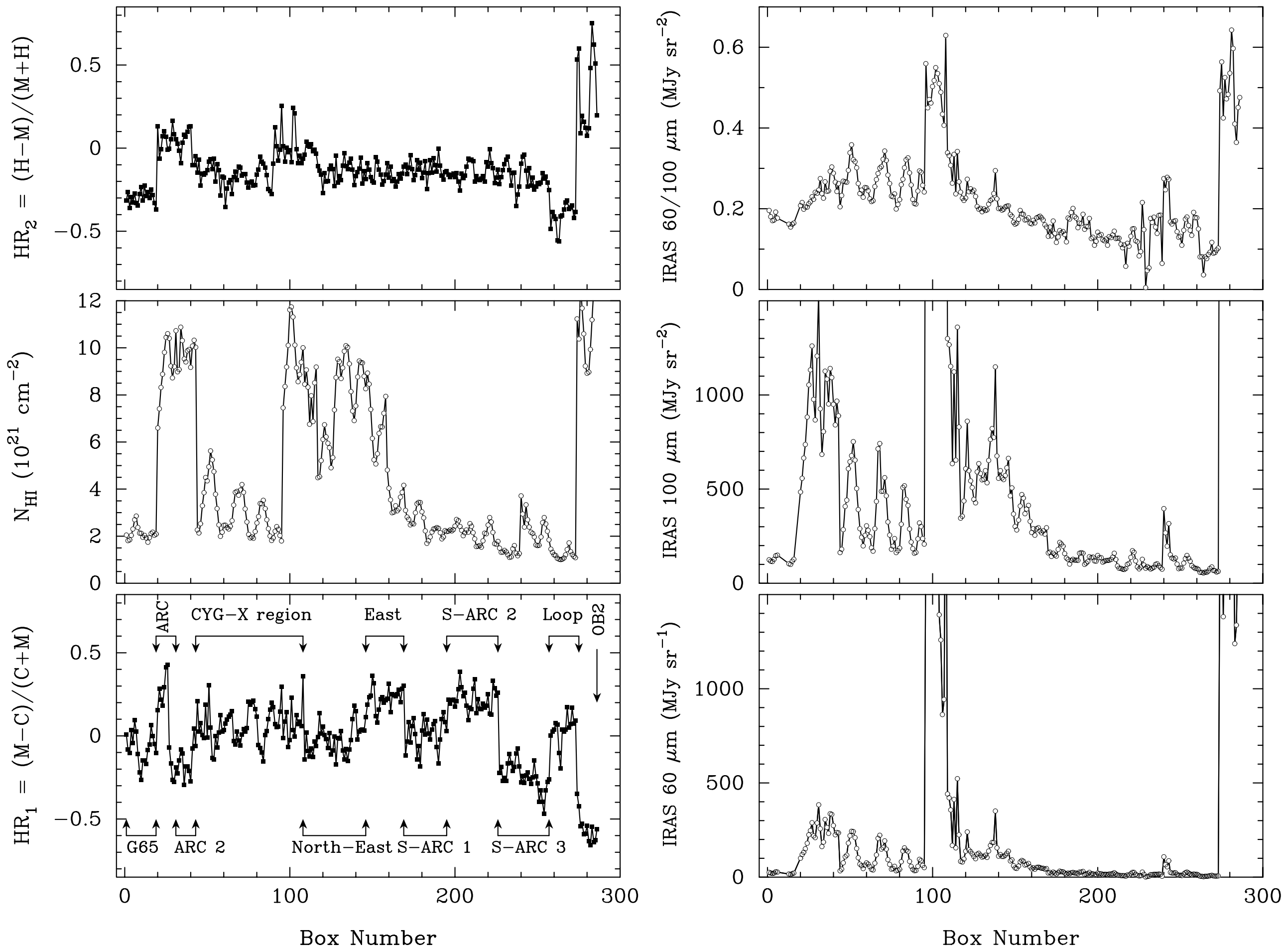

Fig. 14. Comparison of the X–ray hardness ratio distributions with those obtained in the infrared and HI, (see Fig. 13 for the selected regions). The left hand panel displays the distribution of the HR_1, HI and HR_2 in the region, from bottom to top respectively. The right hand panel shows the distribution of the IRAS 60 μm and 100 μm intensities and the 60 μm/100 μm ratio for the same regions as in the left hand panel

material observed in this direction ($N_{\rm H\,I} \simeq 1.8\ 10^{21}$ cm^{-2} and $N_{\rm H_2} \simeq 2\ 10^{19}$ cm^{-2}). The main differences between the southern arcs are visible in the HR_1 distribution. The lowest absorption of the C band emission is found for S-ARC 3, the highest for S-ARC 2. From this we expect distances d of $d_{\rm S-ARC3} < d_{\rm S-ARC1} < d_{\rm S-ARC2}$. This result does not contradict a possible association between S-ARC 3 and the bubble of Cyg OB4.

Cygnus Loop (box-no. 258–273): This region contains large amount of molecular gas ($N_{\rm H_2} \simeq 0.1\ 10^{21}$ cm^{-2}) and shows a soft spectrum ($HR_1 \sim 0 > HR_2$). Optical observations reveal a distance of 440 pc (Blair et al. 1999) thus making a possible connection of this SNR with the rest of the structures unlikely.

OB2 (box-no. 274–286): In the direction of OB2 the hydrogen column density reaches the highest value ($N_{\rm H\,I} \simeq 12.0\ 10^{21}$ cm^{-2} and $N_{\rm H_2} \simeq 5\ 10^{21}$ cm^{-2}). Any object beyond the bulk of this gas should be hidden to the PSPC. However $HR_1 << 0$ indicates a very soft spectrum where HR_2 shows a very hard one ($H > C > M$). Hence, the C band intensities do not suffer much from the absorption. Emission at this band is probably related to the Cygnus Rift and only the emission at higher energies is associated with the environment of the OB2 association. The absorbing material is spread over large radial velocities down to at least -90 km s^{-1}, corresponding to distances of several kpc. Most of this gas does not contribute to the absorption, because of the distance of OB2 of <2.1 kpc (see Table 1). Only material at low positive velocities contribute to the absorption. But this will hardly affect the M band emission.

In brief, we observe X–ray emission with a relatively soft spectrum in areas with low absorption by intervening material. In most regions there is high $N_{\rm H\,I}$ column density and low HR_1 due to absorption. When soft X–ray emission is seen, a significant fraction of the interstellar gas should be located behind the emitting region.

The molecular column density reaches up to $5\ 10^{21}$ cm^{-2} towards OB2. This is enough to absorb the M band emission. The molecular content of the region should be the major absorber (see also Fig. 18) for the X–rays giving the horse-shoe shape of the CSB, which is at a larger distance than the absorbing molecular gas. The reason that we still receive emission from S117 is most

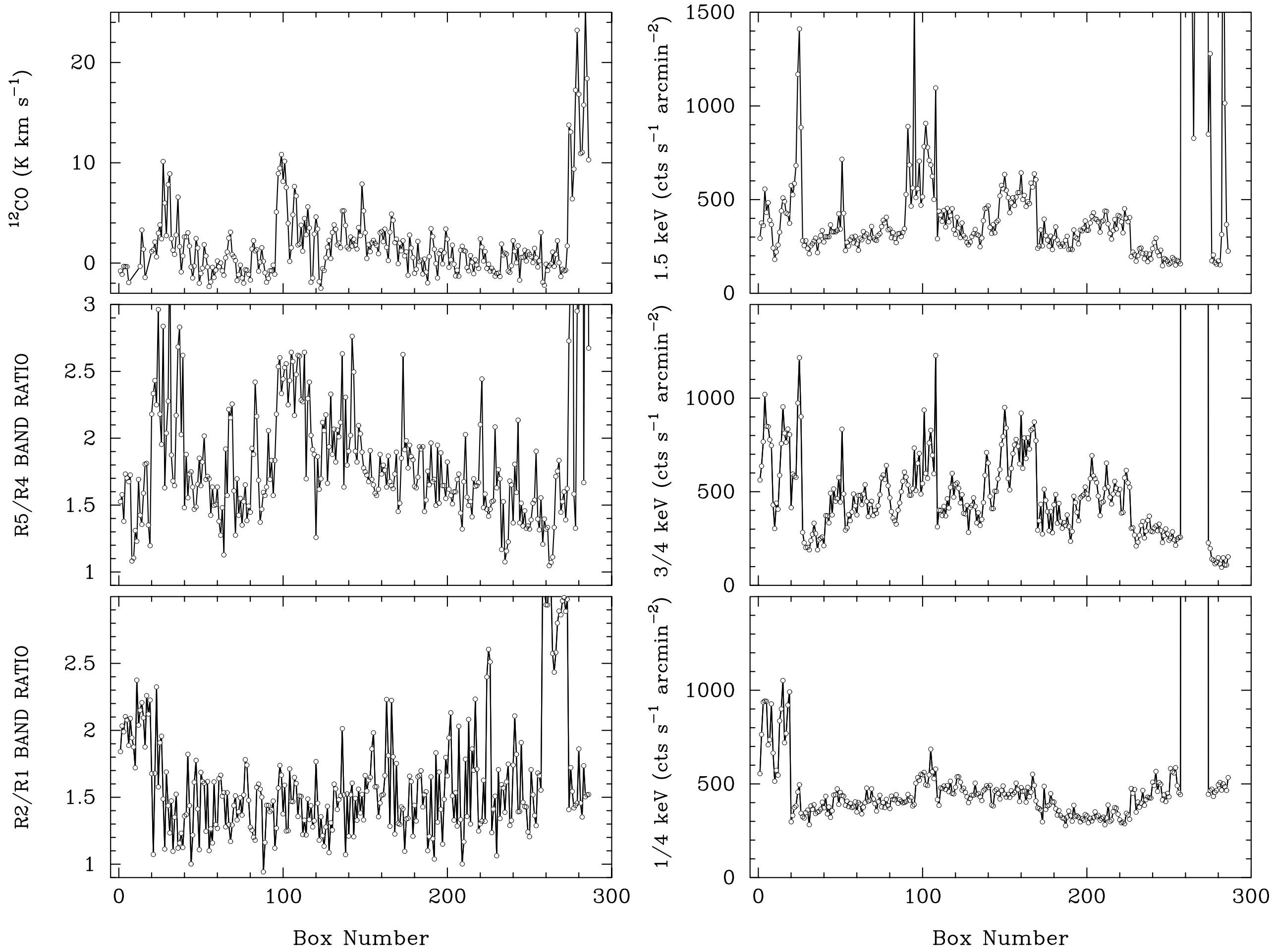

Fig. 15. Same as Fig. 14 but for the $R2/R1$ and $R5/R4$ band ratios of the PSPC and for the CO map integrated between -20 to 20 km s^{-1} (left hand panel). The band ratios trace the temperature variations. The right hand panel shows the distributions for the 1/4, 3/4 and 1.5 keV energy bands

likely due to its small distance (~0.5–0.8 kpc), which is comparable to that of the Cygnus Rift, with less absorbing material in front of it ($N_{\rm H_2} \sim 6\ 10^{20}\,{\rm cm}^{-2}$).

8. H I structures

The CSB is seen along the line of sight towards the Orion local arm. According to McCutcheon & Shuter (1970) the arm region extends up to 4 kpc in the line of sight. The Galactic rotation curve, within 5 kpc, gives velocities $\lesssim |20|$ km s^{-1} (Burton 1988). Due to the velocity distribution of the H I gas, McCutcheon & Shuter (1970) conclude that the structures with a velocity of $V_{\rm LSR} \gtrsim -30$ km s^{-1} and $V_{\rm LSR} \lesssim 10$ km s^{-1} are located in the Orion arm. The typical velocities for the Perseus arm, for the longitude interval of interest, are between -70 to -30 km s^{-1}. Although it is difficult to determine the distances in this region due to our tangential view, it is possible to discriminate the structures according to their velocities. Note that positive velocity of a structure in this region indicates that this structure is in the solar vicinity.

There was a claim that the H I supershell G81$-$5 (diameter 13°) found by Heiles (1979) is connected to the CSB (Cash et al. 1980). The radio map and the ROSAT survey data do not show any structure coincident with this H I supershell. According to Heiles (1979) the shell has a distance of 7.5 kpc and thus belongs most likely to the Perseus arm.

8.1. Some individual H I structures

Besides providing information on the absorbing material of the Cygnus region, the H I data from the Dwingeloo survey show several interesting emission structures. Some of these structures are briefly discussed in this section, starting from the most negative velocities.

Here we discuss some features not visible in Fig. 7, but which may be related to the Cygnus structures. Note, however, that velocities of $\lesssim -20$ km s^{-1} are actually signatures of H I structures in the Perseus arm and are only of relevance, if they are due to peculiar velocities.

The Cygnus region, in virtue of H I structures, is empty at the lower velocity range (-300 to -175 km s^{-1}) and the first structures appear at about a velocity of $V_{\rm LSR} \sim -150$ km s^{-1}. These are: a blob of emission with a size of about 5° × 4° at $\ell \sim 63\overset{\circ}{.}5$, $b \sim 13\overset{\circ}{.}5$ and an H I-arc

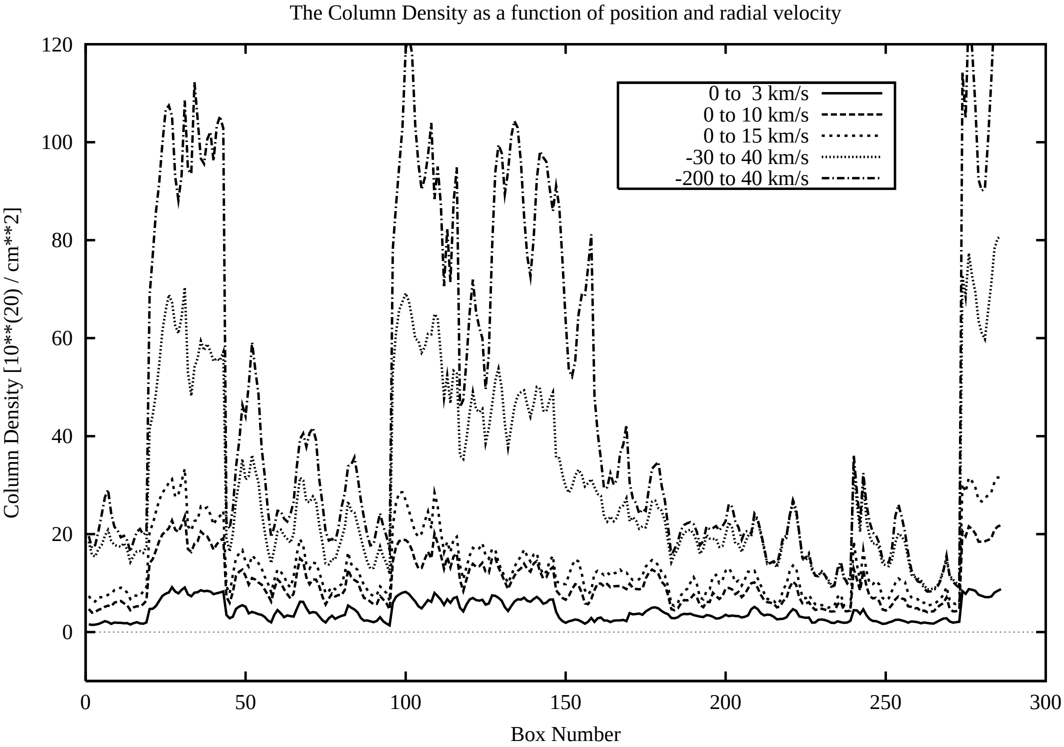

Fig. 16. Variation of the H I column density across the selected boxes as a function of radial velocity. The legend shows the corresponding velocity intervals

passing south of HB21. This arc extends to higher longitudes and merges with the bulk of the high velocity structure beyond $\ell = 100°$ (Perseus arm). At these negative velocities all emission structures are located in the eastern part of the CSB towards Cyg OB7 indicating a further structural difference across the CSB. With increasing velocity the high-velocity arc extends towards the west and merges with a emission blob at about $V_{\rm LSR} \sim -100$ km s^{-1}. A large arc is formed running parallel to the Galactic plane covering the entire Cygnus region in a similar way as can be seen in the X–ray and radio images.

The H I map displayed in Fig. 17 shows a shell-like structure around $\ell \sim 91°$ and $b \sim -4°$. This structure has a size of $7° \times 9°$ in ℓ and b, respectively and was included in the list of Heiles (1979) as a stationary H I shell. According to Heiles (1979) this shell-like structure is at a distance of 9 kpc. The nearby association Cyg OB7 is located in the north of this shell. There are three O stars and three WR stars within the shell. The O stars are HD 202124, an O9 star at a distance of 4.1 kpc, and BD +4 3591, an O type star with a distance of 2.2 kpc, and HD 203064, an O7 star just 0.8 kpc away. Interestingly, there is coinciding X–ray emission S-ARC 1 (Sect. 7.3) located within this shell-like structure. It is difficult to judge whether these stars are associated with the X–ray structure. This structure can be traced up to a velocity of -55 km s^{-1}. In the H I maps (Figs. 7–8) a shell-like structure similar to this one can also be seen at the same coordinates. Due to kinematical arguments it should be closer than 1 kpc. However the bubble at $-75 \leq V_{\rm LSR}$ (km s^{-1}) ≤ -50 (Fig. 17) is most probably in the Perseus arm.

At -25 km s^{-1} an arc like structure, coinciding positionally with the southern arc in the radio and IRAS ratio images, becomes visible. Kinematically this arc should be a local feature.

Towards positive velocities we see higher column densities in the west than in the east along the galactic plane, just in contrast to the negative velocity regime, and the high intensity region of the radio map towards $\ell = 78°$, $b = 2°$ becomes distinct. At $V_{\rm LSR} \sim 50$ km s^{-1} and beyond all structures disappeared and no new features show up.

To summarize: there exist some shell or bubble-like structures in the H I channel maps. Most of them show no corresponding structures at other wavelengths. The H I gas distribution is an important tracer of the absorbing regions shaping the observed X–ray structures and in particular absorbing the central region of the CSB. Apart of that, no sign for a relation of emission or absorption structure with the X–ray structures is found. The distribution of the H I gas shows no evidence for a coherent structure comparable in size to the CSB.

9. CO structures

From the preceding discussion it is clear that the shape of the CSB, its horse-shoe like appearance in particular, is due to absorption by the interstellar medium, where the CO emission is a tracer of cold and dense gas.

Discrete CO structures are visible between -10 km s^{-1} and $+10$ km s^{-1} (see Fig. 10). At velocities smaller than

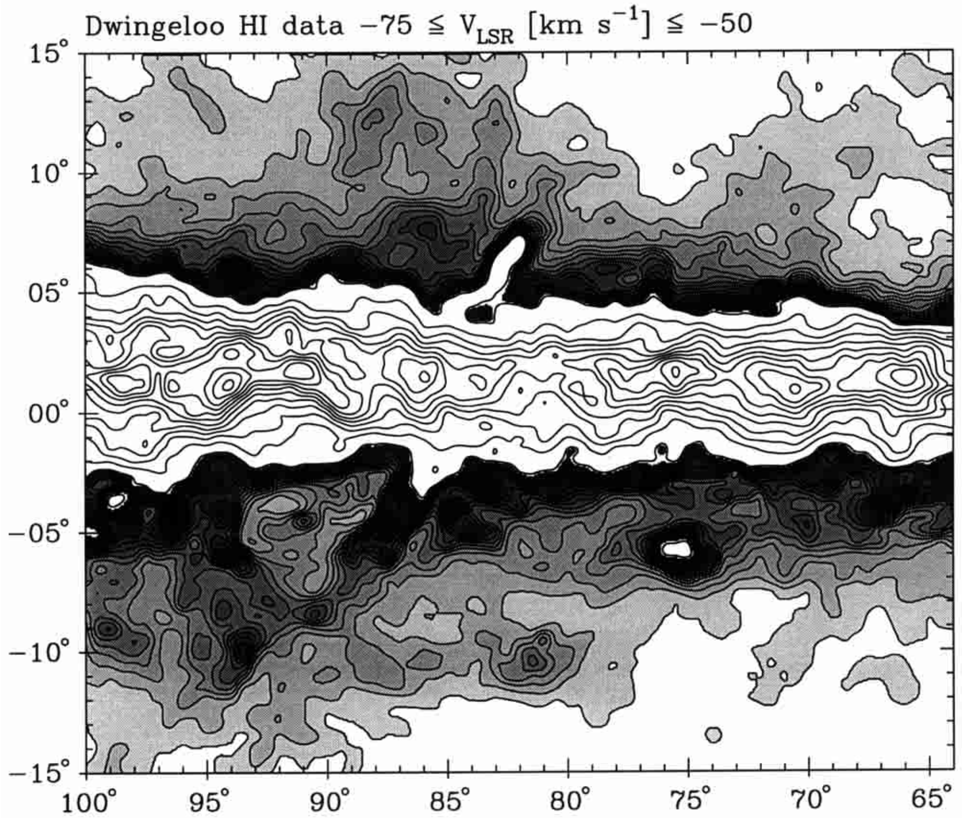

Fig. 17. The $N_{\rm H\,I}$ column density, at velocities corresponding to the Perseus arm, across the Cygnus region from the Dwingeloo HI survey shown as contour map. The shaded contours are plotted starting at 0.3 10^{20} cm^{-2} in steps of 0.3 10^{20} cm^{-2}. The contours corresponding to the Galactic plane (unshaded region) start at 5 10^{20} cm^{-2} and are plotted in steps of 3 10^{20} cm^{-2}

-12 km s^{-1} there exists large scale diffuse CO emission. The CO-maps in Fig. 10 show structures at negative velocities at about $\ell \sim 90°$ close to the Cyg OB7 association, which disappears beyond about $+5$ km s^{-1}. CO emission towards Cyg X is visible in the velocity range above -5 km s^{-1} in Fig. 10 and coincides well with the absorbed part of the X–ray image.

There exist two major groups of absorbing material. One spatially coincides with the Cyg OB7 and the other coincides with the Cygnus Rift. The two major groups seem connected by emission at -0.6 km s^{-1}, where there is less X–ray emission. According to their different kinematics both structures seem physically unrelated.

The CO image in the $-4.5 \leq V_{\rm LSR}({\rm km\ s^{-1}}) \leq 3.3$ interval is shown in Fig. 18 with superimposed 3/4 keV X–ray emission. This image shows that local material absorbs the X–rays emission from this region. An asymmetry exists in the CO distribution with respect to the X–ray emission showing the southern X–ray ridge nearly free from absorbing material.

10. The nature of the Cygnus superbubble

The first arguments against an explanation of the Cygnus superbubble being a single object were given by Bochkarev (1984) and Bochkarev & Sitnik (1985). The main argument is related to the size and shape of the observed X–ray structure and individual sources in the region. Their properties are known to a large extent. They provide a persuasive support to the argument.

The CSB extent along the Galactic plane (18°) exceeds that across the plane (14°). Regarding the shape of the structure, Bochkarev (1984) argues that, if the structure is larger in diameter than the gaseous Galactic disk (200–300 pc), one expects the superbubble to extend farthest across the Galactic plane, like the Orion-Eridanus bubble. This argument is also supported by numerical bubble models (i.e., Mac Low et al. 1989; Tomisaka 1998).

The most prominent part of the Cygnus region in radio wavelengths (Cyg X), proposed to be related to the superbubble, consists most likely of physically unrelated sources (Dickel & Wendker 1978; Wendker 1984; Piepenbrink & Wendker 1988). The S117 complex (Pelican and North America nebulae) is associated with a local molecular cloud at a distance of ∼0.7 kpc and is not part of the CSB. The southern arm of the CSB towards $\ell \sim 85°$, $b = -7°$ is most likely related to the bubble produced by Cyg OB4, which is at a distance of 1 kpc.

Parts of the horse-shoe shaped X–ray emission have different distances and thus it is unlikely a physically coherent structure.

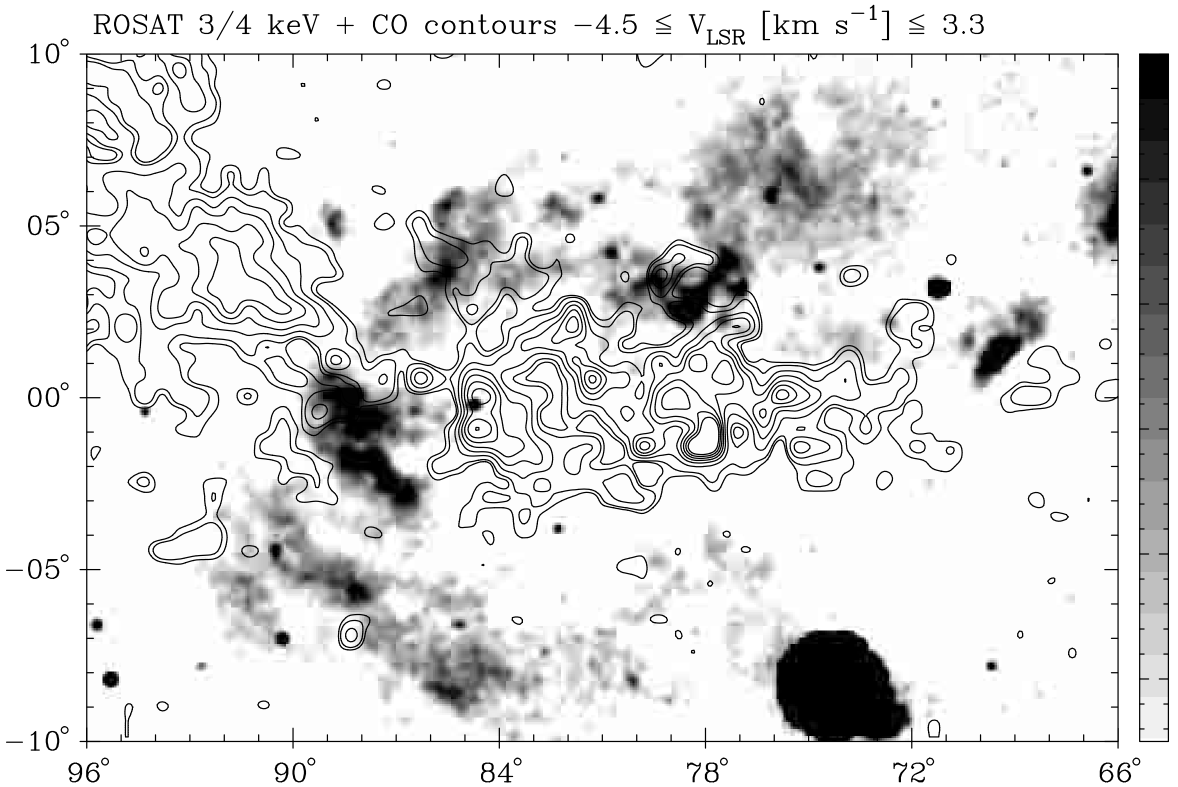

Fig. 18. This figure displays the CO data in the interval $-4.5 \le V_{\rm LSR}$ (km s^{-1}) ≤ 3.3 in contours plotted on top of the ROSAT 3/4 keV image. It is apparent that the absorbing material is distributed mostly at velocities close to zero. Note that there exist a remarkable anticorrelation between the very local CO gas and the X–ray data

11. Conclusion

We have analyzed the Cygnus region containing the remarkable X–ray structure known as the CSB using new radio continuum and X–ray data together with existing data at other wavelengths. This analysis provides new information on the nature of the structures towards the Cygnus region. Since the discovery of the CSB by the A-2 HEAO-1 data of Cash et al. (1980) several attempts have been made to understand the structure and energetics of this huge emission region.

The findings of this paper can be summarized as:

- The OB2 association is not at the center of the CSB as previously quoted (Fig. 1);
- The distribution of the other OB associations shows that only some of them partly correlate with the whole structure;
- Most of the soft X–ray emission (1/4 keV) is not related to the X–ray structures which forms the CSB, but to a local and quite large, tilted emission belt;
- The southern X–ray ridge of the CSB seems not to be related to the other X–ray structures. This arm is not spatially correlated with the radio continuum emission but with the infrared emission. The radio arm envelopes both the X–ray and infrared structures and has a counterpart in H I emission;
- The IRAS ratio map shows a very large elliptically shaped structure, visible in Fig. 9;
- H I emission across the CSB is not uniformly distributed. Surprisingly, the north-east region has higher hydrogen column density than the Cygnus X region. The expectation from a bubble, however, is to expand in the direction of lower column density regions;
- Molecular gas seems to be playing a major role in forming the horse-shoe shape of the CSB;
- In almost all of the images it is possible to find numerous arc, loop or bubble-like structures arbitrarily distributed over the whole region;
- The molecular gas forming the Cygnus Rift splits into two major groups positionally and kinematically the two parts have different distances;
- A spherical bubble, approximately at the position of OB4, fits the X–ray bay of the southern arc. Due to the absorption argument and distances of the OB stars in this region it seems that they are physically connected;
- The north-east and southern parts of the CSB has a lower dust temperature than the rest of the CSB.

The general picture of the Cygnus region can be explained as follows: we are looking through a cylinder with numerous objects at different distances. This cylinder is the Orion local arm oriented tangentially along the line of sight. Its axis is at $\ell \approx 77°$ and our perception of the

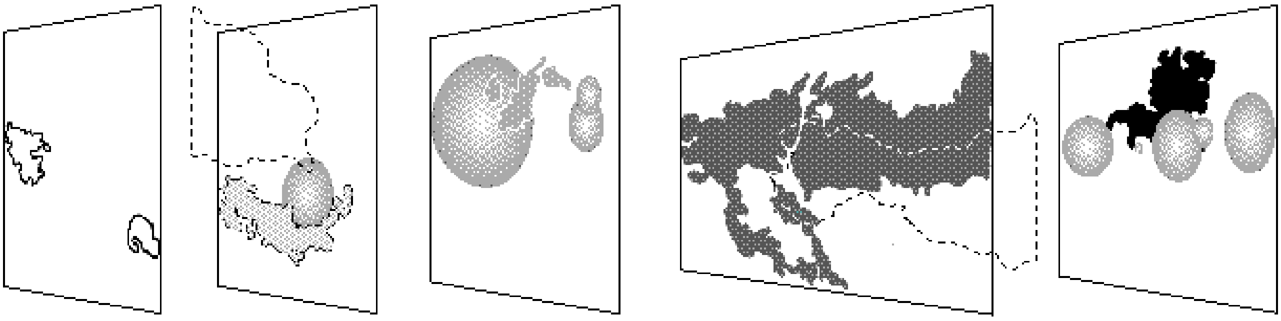

Fig. 19. A sketch of the Cygnus region based on the local arm distribution model, drawn not to scale, although the relative sizes of the structures are kept. Each plane is positioned according to its distance; the left hand plane is closest to us. Since no distance to the radio continuum structures has been assigned, the fourth plane is arbitrarily placed between the foreground structures and the Cygnus X-region. In our interpretation we are looking into the spiral arm and CSB is just an illusion. Thus the plane at the very left shows the nearest structures which are the North America and Pelican complex together with the Cygnus loop. The next plane displays the eastern part of the Cygnus Rift, the southern X–ray arm associated with OB4 (shown by a sphere). The third plane shows the north-east part of the CSB together with OB1, OB7 and OB9. Note that the second and third planes show objects at similar distances. The fourth plane shows the outer contours of the radio emission and the western part of the Cygnus Rift. Here the Rift might extend up to 2 kpc. Since the distance of the radio structures are not known but it would be difficult to explain their sizes for distances >2 kpc, the radio contours are also placed in this plane. As we look further we see more distant objects. The right-most plane shows the remaining OB associations and the rest of the CSB

shell or bubble-like structures is most likely affected by our tangential line-of-sight into the spiral arm.

The circular shape of the bubble is due to radiation from the spiral arm, where the absorbing material towards the central area shapes the feature. Towards the Cygnus region we expect bubbles created by OB associations and in addition several H II bubbles should be seen too. Our data, however, support the view that a superposition of several bubbles and shells in the Cygnus region is seen rather than a single object. We summarize our discussion by sketching our view of the Cygnus region in Fig. 19. According to this, the Cygnus Loop and S117 complex are closest. Then comes the eastern part of the Cygnus Rift followed by the southern arc and OB4 bubble. OB7 together with the north-east part come next. After this distance at about 1.2 kpc we place the western part of the Cygnus Rift. Cygnus X and the other OB associations are the most distant and complete the picture.

Acknowledgements. We thank Carl Heiles, Lloyd Higgs and Patricia Reich for critical reading of the manuscript.

References

Abbott, D. C., Bieging, J. H., & Churchwell, E. 1981, ApJ, 250, 645

Arendt, R. G., Dwek, E., & Leisawitz, D. 1992, ApJ, 400, 562

Aschenbach, B. 1988, Appl. Opt., 27, 1404

Aschenbach, B. 1993, Adv. Space Res., 13, 12, 45

Beichmann, C. A., Neugebauer, G., Habing, H. J., Clegg, P. E., & Chester, T. J. 1985, IRAS Explanatory Supplement

Berkhuijsen, E. M. 1973, A&A, 24, 143

Blair, W. P., Sankrit, R., Raymond, J. C., & Long, K. S. 1999, ApJ, 118, 942

Bloemen, J. B. G. M., Deul, E. R., & Thaddeus, P. 1990, A&A, 233, 437

Bochkarev, N. G. 1984, Sov. Astron. Lett., 10, 2

Bochkarev, N. G., & Sitnik, T. G. 1985, ApSS, 108, 237

Bowyer, C. S., Field, G. B., & Mack, J. E. 1968, Nature, 217, 32

Bregman, J. N. 1980, ApJ, 236, 577

Brand, J., & Blitz, L. 1993, A&A, 275, 67

Brouw, W. N., & Spoelstra, T. A. Th. 1976, A&AS, 26, 129

Brown, A. G. A., Hartmann, D., & Burton, W. B. 1995, A&A, 300, 903

Brown, A. G. A., Dekker, G., & de Zeeuw, P. T. 1997, MNRAS, 285, 497

Burton, W. B. 1988, in Galactic and Extragalactic Radio Astronomy, ed. G. L. Verschuur, & K. I. Kellermann (Springer Verlag), 351

Cash, W., Garmire, G., & Riegler, G. 1980, ApJ, 238, L71

Castor, J., McCray, R., & Weaver, R. 1975, ApJ, 200, L107

Chen, W., White, R. L., & Bertsch, D. 1996, A&AS, 120, 423

Comerón, F., Torra, J., Jordi, C., & Gómez, A. E. 1993, A&AS, 101, 37

Comerón, F., Torra, J., & Gómez, A. E. 1998, A&A, 330, 975

Cox, D. P., & Smith, B. W. 1974, ApJ, 189, L105

Dame, T. M., Ungerechts, H., Cohen, R. S., et al. 1987, ApJ, 322, 706

de Zeeuw, P. T., Hoogerwerf, R., de Bruijne, J. H. J., Brown, A. G. A., & Blaauw, A. 1999, AJ, 117, 354

del Rio, E., von Ballmoos, P., Bennett, K., et al. 1996, A&A, 315, 237

Dickel, H. R., Wendker, H. J., & Bieritz, J. H. 1969, A&A, 1, 270

Dickel, H. R., & Wendker, H. J. 1978, A&A, 66, 289

Egger, R. 1998, in Proc. IAU Coll. 166, The Local Bubble and Beyond, Lect. Notes Phys. 506, ed. D. Breitschwerdt, M. J. Freyberg, & J. Trümper (Springer), 287

Elmegreen, B. G., & Lada, C. J. 1977, ApJ, 214, 725

Feldt, C., & Green, D. A. 1993, A&A, 274, 421

Ferrière, K. M. 1995, ApJ, 441, 281

Ferrière, K. M., MacLow, M.-M., & Zweibel, E. G. 1991, ApJ, 375, 239

Fürst, E., Reich, W., & Sofue, Y. 1987, A&AS, 71, 63

Garmany, C. D., & Stencel, R. E. 1992, A&AS, 94, 211

Green, D. A. 2000, A Catalogue of Galactic Supernova Remnants (2000 August version). Mullard Radio Astronomy Observatory, Cambridge, UK (available on the World-Wide-Web at `http://www.mrao.cam.ac.uk/surveys/snrs/`

Green, D. A., & Gull, S. F. 1989, MNRAS, 237, 555

Guo, Z., Burrows, D. N., Sanders, W. T., Snowden, S. L., & Penprase, B. E. 1995, ApJ, 453, 256

Hartmann, D., & Burton, W. B. 1997, Atlas of Galactic Neutral Hydrogen (Cambridge University Press, Cambridge)

Haslam, C. G. T., Stoffel, H., Salter, C. J., & Wilson, W. E. 1982, A&AS, 47, 1

Higdon, J. C. 1981, ApJ, 244, 88

Heiles, C. 1979, ApJ, 229, 553

Heiles, C. 1998, ApJ, 498, 689

Humphreys, R. M. 1978, ApJS, 38, 309

Kitamoto, S., & Mukai, K. 1996, PASJ, 48, 813

Landecker, T. L., Purton, C. R., & Clutton-Brock, M. 1990, A&A, 232, 207

Landecker, T. L., Higgs, L., & Wendker, H. J. 1993, A&A, 276, 522

Landecker, T. L., Roger, R. S., & Higgs, L. 1980, A&AS, 39, 133

Landecker, T. L., Routledge, D., Reynolds, S. P., et al. 1999, ApJ, 527, 866

Leahy, D. A., & Aschenbach, B. 1996, A&A, 315, 260

Leitherer, C., Bertout, C., Stahl, O., & Wolf, B. 1984, A&A, 140, 199

Lozinskaya, T. 1981, SvAL, 7, 17

Lozinskaya, T. A., & Repin, S. B. 1990, SvA, 67, 1152

Lozinskaya, T. A., Sitnik, T. G., & Pravdikova, V. V. 1993, AZ, 70, 469

Lucke, P. B. 1978, A&A, 64, 367

Mac Low, M.-M., McCray, R., & Normal, M. L. 1989, ApJ, 337, 141

Massey, P., & Thompson, A. B. 1991, AJ, 101, 1408

McCammon, D., & Sanders, W. T. 1990, ARA&A, 28, 657

McCammon, D., Burrows, D. N., Sanders, W. T., & Kraushaar, W. L. 1983, ApJ, 269, 107

McCutcheon, W. H., & Shuter, W. L. H. 1970, AJ, 75, 910

Mel'nik, A. M., & Efremov, N. Yu. 1995, SvAL, 21, 10

Miller, F. D. 1937, Ann. Harvard Coll. Obs., 105, 297

McKee, C. F., & Ostriker, J. P. 1977, ApJ, 218, 148

Morrison, R., & McCammon, D. 1983, ApJ, 270, 119

Pfeffermann, E., Briel, U. G., Hippmann, H., et al. 1987, Proc. SPIE, 733, 519

Piepenbrink, A., & Wendker, H. J. 1988, A&A, 191, 31

Pyne, A. C. 1960, AJ, 65, 154

Raymond, J. C., & Smith, B. W. 1977, ApJS, 35, 419

Reddish, V. C., Lawrence, L. C., & Pratt, N. M. 1966, Publ. Roy. Obs. Edinburgh, 5, 111

Reich, W. 1982, A&AS, 49, 219

Reich, P., & Reich, W. 1986, A&AS, 63, 205

Reich, W., Reich, P., & Fürst, E. 1990, A&AS, 83, 539

Reynolds, R. J., & Ogden, P. M. 1979, ApJ, 229, 942

Rosen, A., Bregman, J. N., & Kelseon, D. D. 1996, ApJ, 470, 839

Ruprecht, J., Balázs, B., & White, R. E. 1981, in Catalogue of Star Clusters and Associations, Suppl. 1., Part B2, Akadémiai Kiadó, Budapest

Sharpless, S. 1959, ApJS, 4, 257

Sitnik, T. G., & Mel'nik, A. M. 1996, SvAL, 22, 422

Snowden, S. L., Freyberg, M. J., Plucinsky, P. P., et al. 1995, ApJ, 454, 643

Snowden, S. L., Egger, R., Freyberg, M. J., et al. 1997, ApJ, 485, 125

Sofue, Y., & Reich, W. 1979, A&AA, 38, 251

Spitzer, L. 1990, ARA&A, 28, 71

Straižys, V., Goldberg, E. P., Meištas, E., & Vansevičius, V. 1989, A&A, 222, 82

Strong, A. W., Bloemen, J. B. G. M., Dame, T. M., et al. 1988, A&A, 207, 1

Tatematsu, K., Fukui, Y., Landecker, T. L., & Roger, R. S. 1980, A&A, 237, 189

Tomisaka, K. 1990, ApJ, 361, L5

Tomisaka, K. 1998, MNRAS, 298, 797

Tomisaka, K., Habe, A., & Ikeuchi, S. 1980, ApSS, 78, 273

Torres-Dodgen, A. V., Carrol, M., & Tapia, M. 1991, MNRAS, 249, 1

Trümper, J. 1983, Adv. Space Res., 2, No. 4, 421

Uranova, T. A. 1968, SvA, 12, 1041

Uyanıker, B. 1997, Ph.D. Thesis, Bonn University

Uyanıker, B., Fürst, E., Reich, W., Reich, P., & Wielebinski, R. 1998, A&AS, 132, 401

Uyanıker, B., Fürst, E., Reich, W., Reich, P., & Wielebinski, R. 1999, A&AS, 138, 31

Waldron, W. L., Corcoran, M. F., Drake, S. A., & Smale, A. P. 1998, ApJS, 118, 217

Weaver, R. 1979, in Proc. IAU Symp. 84, The Large-scale Characteristics of the Galaxy, ed. W. B. Burton (Reidel, Dordrecht), 295

Weaver, R., Mc Cray, R., & Castor, J. 1977, ApJ, 218, 377

Wendker, H. J. 1970, A&A, 4, 378

Wendker, H. J. 1984, A&AS, 58, 291

Wendker, H. J., & Altenhoff, W. J. 1980, A&A, 92, L5

Wendker, H. J., Higgs, L. A., & Landecker, T. L. 1991, A&A, 241, 551

Young, J. S., Xie, S., Tacconi, L., et al. 1995, ApJS, 98, 219